Lead change of a HIF-2α antagonist guided by multiparameter optimization and utilization of an Olp ⋯ π*Ar interaction

Paul M. Wehn (paul.wehn@gmail.com)
BridgeBio Pharma https://orcid.org/0000-0001-6233-2631

Song Yang
Merck Pharmaceuticals: Merck & Co Inc

Jonas A. Grina
Peloton Therapeutics

James P. Rizzi
Peloton Therapeutics

Stephen T. Schlachter
Peloton Therapeutics

Bin Wang
Peloton Therapeutics

Rui Xu
Peloton Therapeutics

Hanbiao Yang
Peloton Therapeutics

Xinlin Du
Peloton Therapeutics

Guangzhou Han
Peloton Therapeutics

Keshi Wang
Peloton Therapeutics

Robert M. Czerwinski
Peloton Therapeutics

Emily L. Ged
Peloton Therapeutics

Heli Huang
Peloton Therapeutics

Megan M. Halfmann
Peloton Therapeutics

Melissa A. Maddie

Peloton Therapeutics
Emily R. Morton
Peloton Therapeutics
Sarah R. Olive
Peloton Therapeutics
Huiling Tan
Peloton Therapeutics
Shanhai Xie
Peloton Therapeutics
John A. Josey
Peloton Therapeutics
Eli M. Wallace
Peloton Therapeutics

Research Article

Keywords: HIF-2α, n π*, transcription factor inhibition, structure based drug design, PT2977, MK-6482

Posted Date: April 10th, 2023

DOI: https://doi.org/10.21203/rs.3.rs-2753648/v1

Lead change of a HIF-2α antagonist guided by multiparameter optimization and utilization of an $O_{lp} \rightarrow \pi^*_{Ar}$ interaction

Paul M. Wehn,*[1] Song Yang,[2#] Jonas A. Grina,[1] James P. Rizzi,[1] Stephen T. Schlachter,[1] Bin Wang,[1] Rui Xu,[1] Hanbiao Yang,[1] Xinlin Du,[1] Guangzhou Han,[1] Keshi Wang,[1] Robert M. Czerwinski,[1] Emily L. Ged,[1] Heli Huang,[1] Megan M. Halfmann,[1] Melissa A. Maddie,[1] Emily R. Morton,[1] Sarah R. Olive,[1] Huiling Tan,[1] Shanhai Xie,[1] John A. Josey,[1] Eli M. Wallace[1]

* paul.wehn@bridgebio.com, ORCID 0000-0001-6233-2631

ORCID 0000-0003-3616-6304

Abstract

Pharmacokinetic properties of our first-generation HIF-2α antagonist PT2385, including modest solubility, resulted in a high recommended phase 2 dose (RP2D) of 800 mg BID and motivated the pursuit of novel scaffolds which could improve solubility and formulation parameters with the goal of improved pharmacokinetics. Herein we disclose our successful efforts to identify such HIF-2α antagonists through an optimization strategy characterized by: (1) increasing the fraction of sp^3 hybridized carbons (Fsp^3), (2) replacing the aromatic portion of the indane core with pyridine heterocycles, and (3) improving a putative $O_{lp} \rightarrow \pi^*_{Ar}$ interaction, an underutilized electrostatic contact in medicinal chemistry. These efforts emphasize the importance of

[1] Peloton Therapeutics Inc., Dallas, TX 75235, a subsidiary of Merck & Co., Inc., Kenilworth, NJ 07033, USA
[2] Merck Research Laboratories, South San Francisco, CA 94080, USA

employing multiple strategies in parameter optimization. In isolation, modifications to areas (1) and (2) improved solubility, but with the compromise of reduced potency. In area (3), understanding the importance of an $O_{lp} \rightarrow \pi^*_{Ar}$ interaction, as documented through a wealth of crystal structures and retrospective calculations, proved essential in guiding SAR and identifying the trifluoromethyl group as a suitable replacement of the sulfone. Only by combining these three strategies could inhibitors with substantially improved solubility and comparable potency be discovered. Finally, the overall improvement in pharmacokinetic properties of the newly identified inhibitors is highlighted through a battery of ADME and in vivo data, including use of pharmacodynamic biomarkers indicative of HIF-2α antagonism.

Graphical Abstract

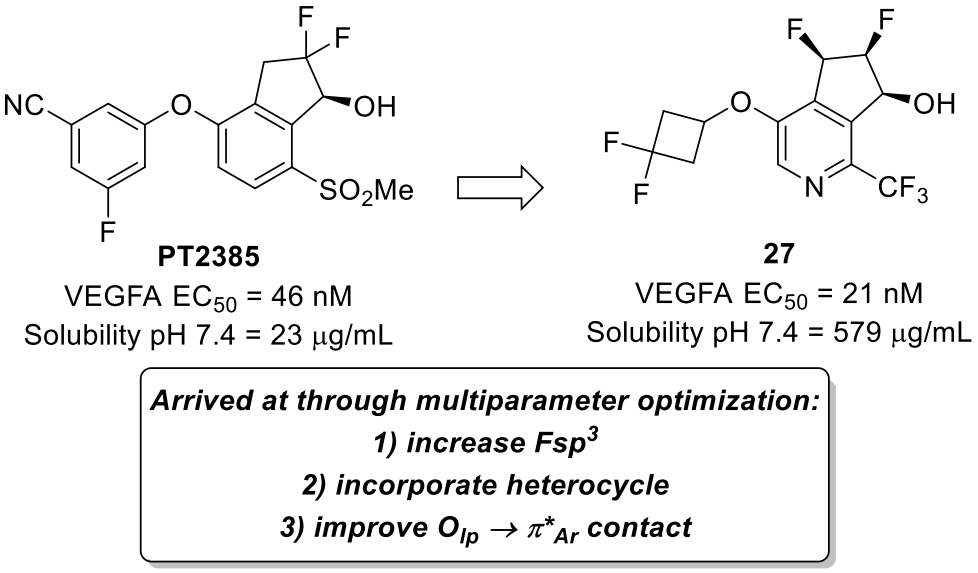

Keywords HIF-2α, $n \rightarrow \pi^*$, transcription factor inhibition, structure based drug design, PT2977, MK-6482

Introduction

Approximately 79,000 patients in the United States were diagnosed with kidney cancer in 2022 . This number represents 4.1% of new cancer diagnoses and places kidney cancer among the 10 most frequently diagnosed cancers. While significant advances in targeted therapies and immunotherapies for the treatment of kidney cancer have been achieved [1], obstacles remain with the 5-year survival rates for advanced or metastatic disease at only 15% [2].

Of kidney cancers, renal cell carcinoma (RCC) is the most common type (90%) and within RCC the most frequent subtype is clear-cell renal cell carcinoma (ccRCC) which accounts for 70% of RCC diagnoses [1]. A particular feature of ccRCC (>90%) is genetic predispositions, somatic mutations, or methylations leading to the inactivation of the tumor suppressor von Hippel-Lindau (VHL) [3]. The VHL protein (pVHL), a substrate adaptor of the E3 ubiquitin ligase complex, mediates the recognition of hydroxylated hypoxia inducible factor α (HIFα) by the ubiquitin ligase complex to enable ubiquitylation of HIFα and subsequent proteasomal destruction [4, 5]. pVHL regulation of HIFα levels thereby controls the cellular response to hypoxic stress. Under normoxia, specific proline residues on HIFα become hydroxylated by oxygen-dependent dioxygenase HIF-specific prolyl-hydroxylases (PHDs) to create a recognition site for pVHL to facilitate the destruction of HIFα. However, under hypoxic conditions this hydroxylation ceases and HIFα accumulates. In the case of ccRCC where pVHL is inactivated, HIFα will accumulate even under normoxia.

The HIF family of transcription factors is composed of three α-isoforms: HIF-1α [6], HIF-2α (EPAS1) [7], and the less characterized HIF-3α [8, 9]. The accumulation of HIFα proteins causes their translocation into the nucleus where they dimerize with the constitutively expressed aryl hydrocarbon receptor nuclear translocator (ARNT, also known as HIF-1β) to form

the active HIF transcription factor complex. The importance of the HIF transcription factor stems from its role coordinating the hypoxic response through the transcription of hypoxia-response elements (HREs) on target genes resulting in the expression of hundreds of genes affecting a suite of responses including anaerobic metabolism, angiogenesis, cell proliferation and survival, immune evasion, extracellular matrix remodeling, pH homeostasis, amino acid and nucleotide metabolism, and genome stability [10-12]. Unsurprisingly, given the accumulation of HIF under normoxic conditions in ccRCC, HIF driven transcriptional activation plays a prominent role in tumor growth. Evidence from studies using HIFα knockdown, VHL reintroduction, or stabilized HIFα variants implicate the HIF-2α isoform as the tumorigenic driver in ccRCC [13-18]. Selective small molecule antagonism of HIF-2α could therefore have important applications in the treatment of ccRCC.

A promising result towards this goal, came from pioneering work by Bruick and Gardner showing that HIF-2α contains an occluded hydrophobic cavity that can bind small molecules and in turn impact dimer formation with ARNT [19-23].[3] Building upon these seminal discoveries, our own investigations identified a novel series of selective indanol based HIF-2α antagonists which bind to the occluded cavity and cause subtle perturbations of the protein architecture [24-26]. The resulting change in the surface of HIF-2α is sufficient to inhibit the dimerization with HIF-1β (ARNT) that forms the HIF transcription factor. The consequent suspension of the HIF transcriptional repertoire by small molecule antagonism generated compelling biochemical and in vivo data which led to the nomination and advancement of PT2385 (Fig. 1), our first-generation HIF-2α antagonist, into clinical trials for patients with previously treated advanced

[3] Although not part of the Gardner and Bruick work, reference 23 shows that agonism of HIF-2α can also be achieved by small molecule binding to the occluded cavity.

ccRCC. While results from the trial were promising, including demonstration of anti-tumor activity and good tolerability, variability in patient exposure was observed with ~15-20% of patients showing low exposure [27]. A thorough examination of the metabolism of PT2385 identified glucuronidation via the polymorphic UDP-glucuronyltransferase (UGT) 2B17 as the principal mode of excretion and rationalized the variable exposure. Remarkably, the variable glucuronidation could be substantially reduced by a point change in the fluorination pattern from geminal fluorination to cis-vicinal fluorination [28]. The resulting compound PT2977 (Fig. 1, MK-6482, Belzutifan) became our second-generation candidate and is currently being evaluated in multiple clinical studies for the treatment of cancers either as a single agent or in combination [29, 30]. Recently, PT2977 achieved FDA approval for the treatment of cancers associated with VHL disease [31, 32].

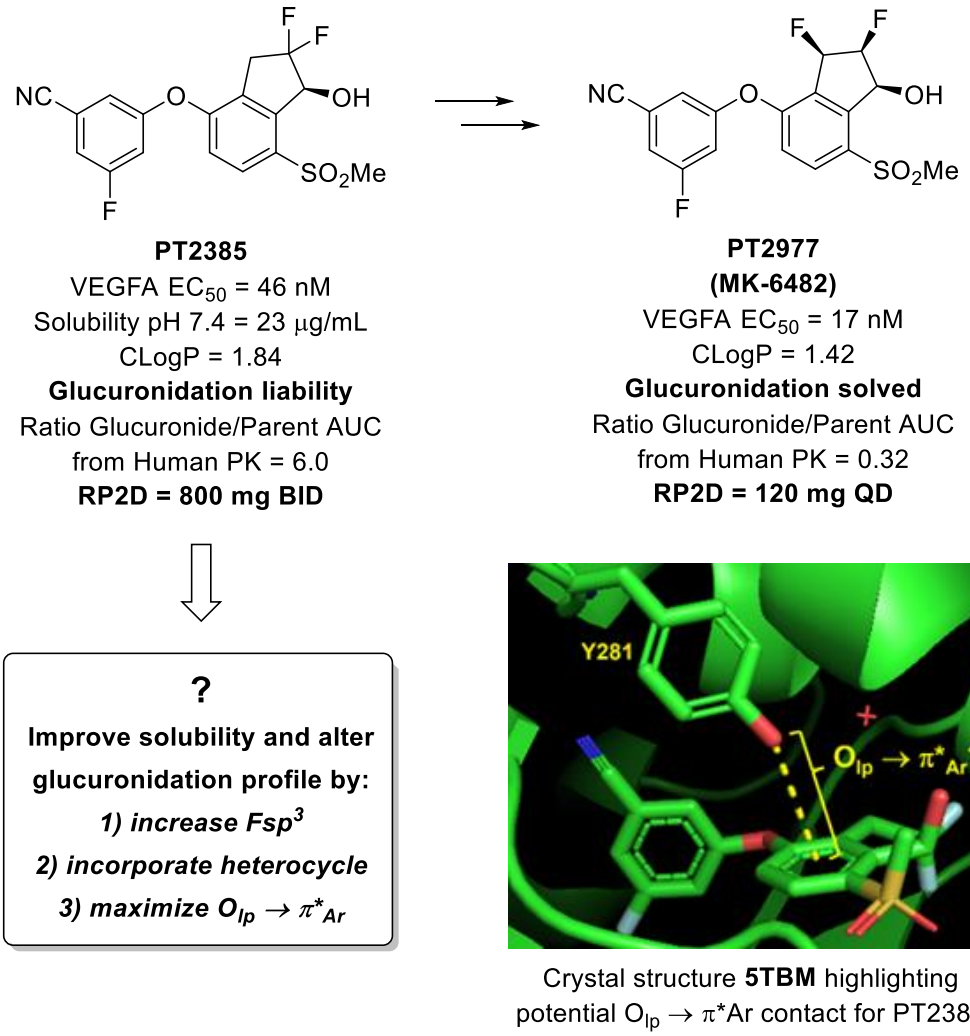

Fig. 1 Rationale for the investigation of HIF-2α antagonists with novel scaffolds and visualization of the $O_{lp} \rightarrow \pi^*_{Ar}$ contact for PT2385

In parallel to the focused optimization efforts which led to the identification of PT2977, we embarked on a broader campaign to change the structure of PT2385. The goal was to address the limited aqueous solubility of PT2385 and potentially alter the intrinsic glucuronidation potential. To resolve these issues, we adopted a 3-pronged approach to modulate properties by focusing on (1) increasing the fraction of sp^3 hybridized atoms (Fsp^3) [33] , (2) incorporating heterocycles into the indanol scaffold [34], and (3) maximizing a potential $O_{lp} \rightarrow \pi^*_{Ar}$ contact [35] (Fig. 1). Highlighted below are the results of our investigations leading to the identification of HIF-2α antagonists with substantially improved aqueous solubility.

Results and Discussion

Approach to increasing the Fsp^3 and the utilization of a putative $O_{lp} \rightarrow \pi^*_{Ar}$ interaction

Given the importance of the indanol alcohol moiety in orchestrating the movement of key amino acid residues in the HIF-2α protein, we retained this feature and sought to increase the Fsp^3 by replacing the benzonitrile moiety with various aliphatic groups. Previous experience with the PT2385 series also indicated a dependence of potency on the electron deficiency of the arene portion of the indanol which increased with the amount of fluorination at the methylsulfonyl group (CH_3SO_2- < FCH_2SO_2 < F_2CHSO_2 < F_3CSO_2-) [26]. Presumably, the observed dependence was a consequence of an $O_{lp} \rightarrow \pi^*_{Ar}$ interaction [35] between the phenolic oxygen lone pair of Tyr281 and the arene π* of the indane; as the arene becomes more electron deficient, the contribution of this electrostatic interaction to binding increases. As we sought to rapidly identify aliphatic replacements to the benzonitrile, a streamlined approach was adopted. First, in order to quickly discover potential aliphatic replacements, we took advantage of the highly electron withdrawing trifluoromethyl sulfone group. While from a physical properties perspective the trifluoromethyl sulfone is not ideal[4], it would facilitate the rapid discovery of aliphatic replacements by enhancing potency thereby enabling thorough SAR evaluation. Second, we utilized a one-pot procedure in which an advanced phenol intermediate was first functionalized with an alcohol by Mitsunobu chemistry and then the silyl group removed to afford the final product (Table 1).

[4] The CLogP for (methylsulfonyl)benzene is 0.74, whereas the CLogP for (trifluoromethylsulfonyl)benzene is 2.91, a difference of ~2.2 log units suggesting that the trifluoromethyl sulfone imparts significant lipophilicity.

Table 1 Results from increasing the Fsp^3 of indanol based HIF-2α antagonists

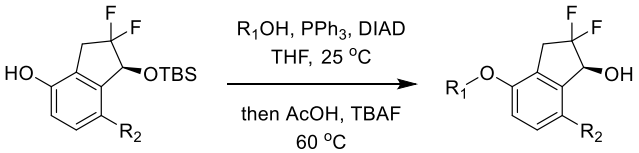

#	R_1	R_2	SPA IC_{50} (nM)	Luciferase EC_{50} (nM)	CLogP
(±)-1	Me	SO_2CF_3	7700	NT	2.62
(±)-2		SO_2CF_3	247	257	3.15
(±)-3		SO_2CF_3	16	11	4.65
4		SO_2CF_3	<5	8.1	3.53
5		SO_2CF_3	88	68	2.87
6		SO_2CF_3	<5	12	3.19
7	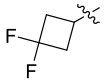	SO_2CF_3	<5	4.2	2.92
8		SO_2CF_3	<5	16	2.25
9	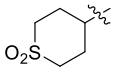	SO_2CF_3	1040	2330	1.85
10	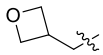	SO_2CF_3	25	75	1.75
11		SO_2CF_3	<5	66	2.49
12	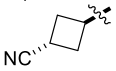	SO_2CF_3	<5	18	2.50
13	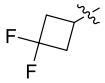	SO_2Me	110	NT	0.81
14	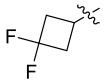	CF3	<5	4.1	3.15

A selection of results from these investigations are highlighted in Table 1. A scintillation proximity assay (SPA) was used as the primary assay to evaluate analogs by measuring displacement of a radiolabeled ligand from the HIF-2α PAS-B* domain [26]. Assessment in the

cell was achieved using a HIF-2α-driven HRE-dependent luciferase assay [26]. In some cases, compounds were further profiled in cell by measuring the secretion of vascular endothelial growth factor A (VEGFA), a well-established target gene of HIF-2α in ccRCC and an alternate marker of cellular activity [26]. Unsurprisingly, replacement of the benzonitrile with small aliphatic replacements was poorly tolerated and showed a strong dependence on size. Both Me (**1**) and Et (**2**) replacements exhibited poor binding affinity which improved with size. Installation of larger cyclic groups, such as cyclohexyl (**3**) and cyclobutyl (**4**), rescued activity with the smaller cyclobutane being more potent. Interestingly, fluorination of the aliphatic groups enhanced activity in both cyclic and non-cyclic derivatives. Fluorination of **2** showed a potency dependence on the amount of fluorination with the mono-fluoro derivative **5** being less potent than the difluoro derivative **6** which showed a ~10-fold improvement in Luciferase activity over **2**. For the cyclobutyl derivative **7**, geminal difluorination imparted only a slight improvement in potency. A larger effort was dedicated to looking at aliphatic replacements that would also impart improved physical properties through the incorporation of heteroatoms. From that screen, it became apparent that groups such as ethers and nitriles were tolerated, while more polar groups such as amides, sulfonamides, and alcohols were not (data not shown) [36].[5] Installation of an oxygen into the cyclohexyl ring of **3**, afforded tetrahydropyran **8** with slightly reduced potency. Switching the ethereal oxygen to a sulfone (**9**) resulted in a substantial loss in binding affinity and is illustrative of the challenges we encountered trying to incorporate more polar elements. Oxetanes were tolerated as demonstrated by **10** and **11**, however, the impact of fluorination on functional activity for this heterocycle was marginal. Finally, a nitrile (**12**) could

[5] Please see reference 36 for additional examples of various polar groups which were tested.

be successfully incorporated into the cyclobutyl ring with only a modest loss in potency compared to the parent cyclobutane **4**.

In order to advance our aliphatic replacements into potential candidates with improved physical properties it would be necessary to replace the highly lipophilic trifluoromethyl sulfone. Given that the most potent aliphatic replacement identified was the 3,3-difluorocyclobutane, we elected to combine this with the methyl sulfone. Unfortunately, the resulting compound **13** was substantially less active. On the plus side, however, the thermodynamic solubility of **13** was 148 μg/mL (pH 7.4) which was a significant improvement over PT2385 (23 μg/mL, pH 7.4).

The switch of sulfones from trifluoromethyl to methyl made us wonder about the contributions of this moiety to binding. Crystallization of trifluoromethyl sulfone **12** (Table 2) revealed that the benzene portion of the indanol formed a close electrostatic contact with the tyrosine phenolic oxygen at 3.3Å possibly maximizing the $O_{lp} \rightarrow \pi^*_{Ar}$ interaction. Past experience with the sulfone moiety in our earlier HIF-2α antagonists (Fig. 2) suggested that a close contact between the arene and tyrosine phenolic oxygen was important for the trifluoromethyl sulfone, but not as much for less fluorinated derivatives. Structurally, this effect manifests as a closer contact between the arene and phenolic oxygen in the trifluoromethyl sulfones and an elongated inferior contact in the case of the less fluorinated sulfones. A panel of crystal structures in Table 2 illustrate this phenomenon. Structurally related compounds **15** and **16** show the differing impacts of trifluoromethyl sulfone and difluoromethyl sulfone moieties. The most obvious difference is that the trifluoromethyl sulfone moiety is rotated 180^o opposite of the difluoromethyl sulfone.[6] The consequence of these opposed orientations is that the arene is

[6] Electron density of the sulfone region for the co-crystal structures in Table 2 unambiguously defines the exhibited rotational isomers.

pushed closer to the phenolic oxygen in the case of trifluoromethyl sulfone **15** (3.5Å) and extended away in the case of difluoromethyl sulfone **16** (3.8Å). While the utility of differences in the tenths of angstroms appears modest in isolation, there is the important arene orientation to consider as well. Comparison of the arene orientations of **15** and **16** suggests that there is likely improved orbital overlap with the phenolic oxygen in **15** (nearly orthogonal angle with the arene plane) than with **16** (more acute angle and the arene surface is tilted away).

The crystal structure of **17**, although lacking an aliphatic group, shows that the same orientation of the difluoromethyl sulfone is preserved for the indanol scaffold. When compared to **12**, the arene orientation of **17** appears inferior being more tilted away from the tyrosine oxygen. Given the importance of a putative $O_{lp} \rightarrow \pi^*_{Ar}$ interaction for aliphatic compounds like **12** and **7**, we wondered whether there might be other groups which could replace the trifluoromethyl sulfone while maintaining the more favorable $O_{lp} \rightarrow \pi^*_{Ar}$ electrostatic contact. Inspiration came from a crystal structure of **18**, which has a trifluoromethyl group in place of the sulfone and shows a similar tyrosine oxygen to arene surface contact as **12**. Interestingly, the overall arene orientation of **18** is more similar to **12** than **17**. Applying this substitution to our aliphatic compounds gave **14** which rescued the potency loss we had observed from methyl sulfone **13**. It is instructive to note the Hammett parameters of the $-SO_2CF_3$ ($\sigma_p = 0.96$), $-SO_2Me$ ($\sigma_p = 0.72$) and $-CF_3$ ($\sigma_p = 0.54$) groups [37], as these values can serve as surrogates for arene electron deficiency. In considering arene electron deficiency alone, one would predict *a priori* that the methyl sulfone would be superior to the trifluoromethyl group. However, the opposite is observed. It seems that the smaller steric size of the trifluoromethyl group facilitates improved arene orientation for the $O_{lp} \rightarrow \pi^*_{Ar}$ contact and thus, improved potency. Our simple heuristic of examining the $O_{lp} \rightarrow \pi^*_{Ar}$ contact to guide structural iteration served as a useful device to

identify the trifluoromethyl group as an equipotent replacement of the trifluoromethyl sulfone. While the lipophilic nature of **14** represented a dead end towards our goal of improved solubility, the observation of rescued potency would prove fortuitous during our examination of heterocycle incorporation into the indane scaffold.

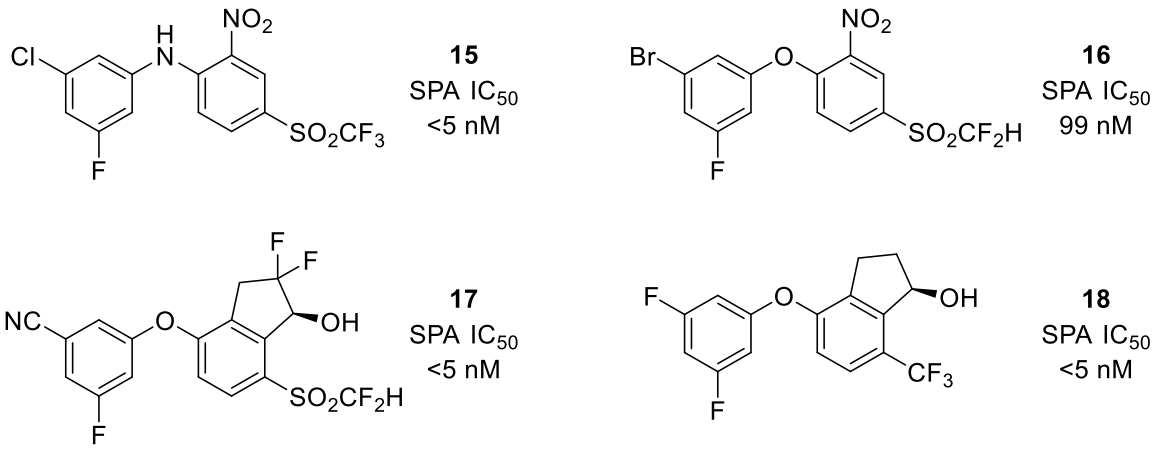

Fig. 2 Historical compounds that were crystallized with the HIF-2α PAS-B*/ARNT PAS-B* dimer and their relevant biochemical/cellular potencies

Table 2 A panel of historical crystal structures highlighting the impact of arene substitution on the putative $O_{lp} \rightarrow \pi^*_{Ar}$ contact

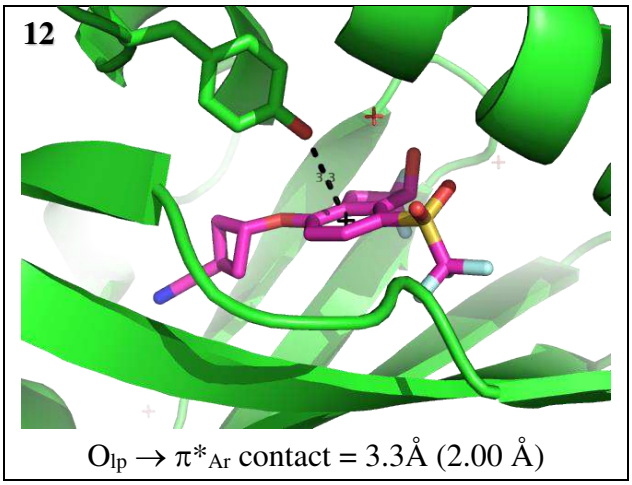

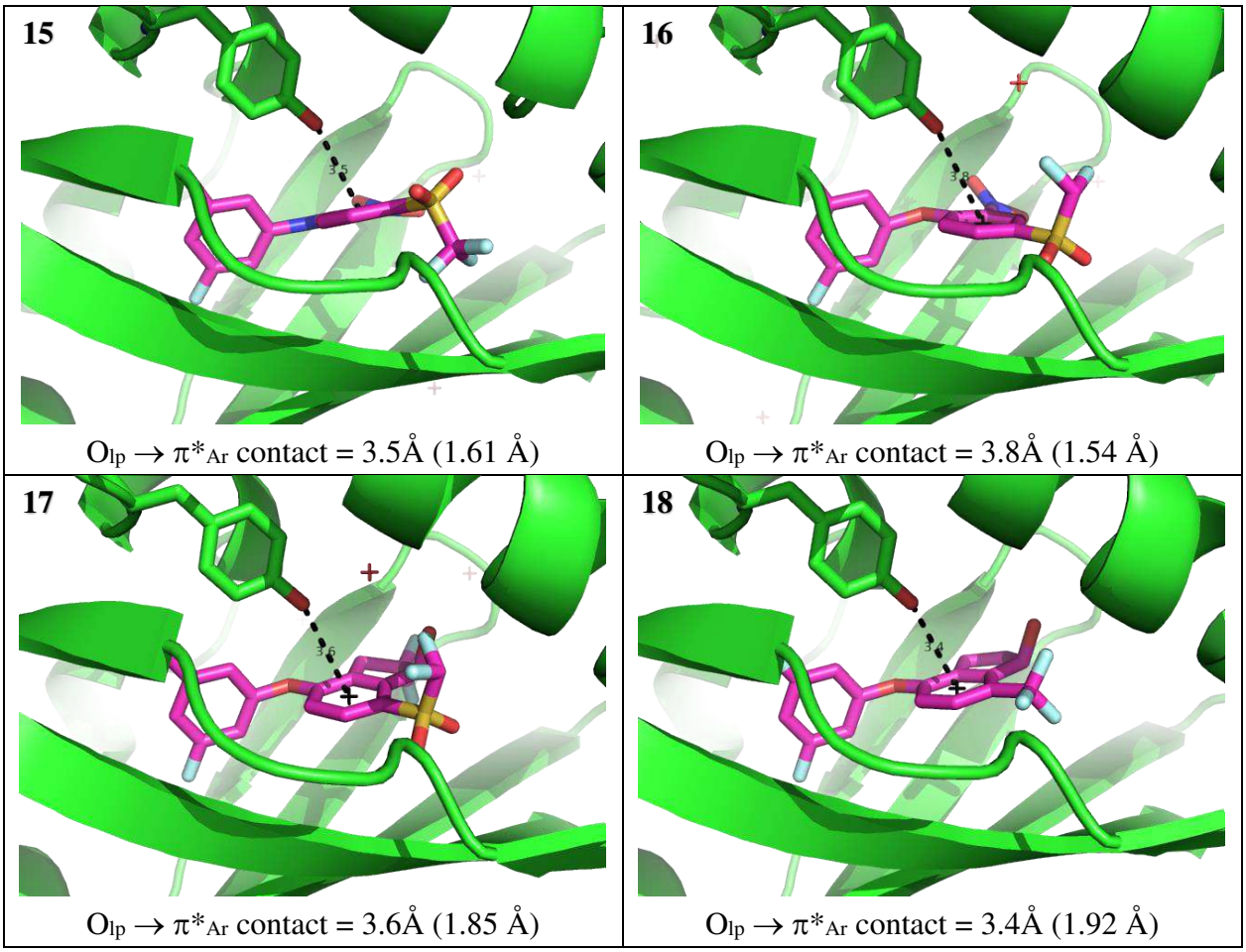

A panel of crystal structures of **12** (PDB code **6X2H**), **15** (PDB code **6D0B**), **16** (PDB code **6X21**), **17** (PDB code **5UFP**), and **18** (PDB code **6X28**) in complex with the HIF-2α PAS-B*/ARNT PAS-B* dimer showing the relevant distance between the oxygen of Tyr281 and the arene centroid (black). The resolution of each crystal structure is shown in parenthesis after the contact distance.

Table 3 Evaluation of nitrogen incorporation at the indane scaffold

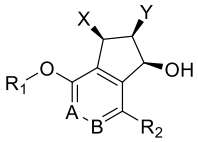

#	R_1	R_2	A	B	X	Y	SPA IC_{50} (nM)	Luciferase EC_{50} (nM)	VEGF EC_{50} (nM)	CLogP
19	3-CN-5-F-C_6H_3	SO_2Me	CH	CH	H	F	41	39	61	1.39
20	3-CN-5-F-C_6H_3	SO_2Me	CH	N	H	F	270	1000	NT	1.31
21	3-CN-5-F-C_6H_3	CF_3	CH	N	H	F	<5	30	51	2.57
(±)-22	3-CN-5-F-C_6H_3	CF_3	N	CH	H	F	2100	NT	NT	2.57
(±)-23	3-CN-5-F-C_6H_3	CF_3	CH	N	H	H	<5	590	NT	2.73
24	3-CN-5-F-C_6H_3	CF_3	CH	N	F	F	<5	7.8	9.3	2.59
25	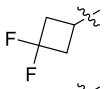	CF_3	CH	N	H	H	41	530	NT	1.72
26	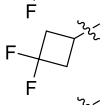	CF_3	CH	N	H	F	<5	23	32	1.56
27	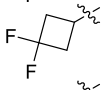	CF_3	CH	N	F	F	NT	10	21	1.59
28	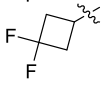	CF_2H	CH	N	H	F	1300	NT	NT	0.78

Replacement of benzene ring with pyridines

Initial exploration of heterocycle incorporation into the indane scaffold proved disappointing (Table 3). The pyridine derivative **20** showed a ~25-fold loss in Luciferase activity from the parent indanol **19**. While this disheartening result initially limited further investigation of heterocycle incorporation, results from the trifluoromethyl benzene derivative **14** encouraged us to revisit pyridine **20**. Replacement of the methyl sulfone in **20** with a trifluoromethyl group afforded **21** whose activity was comparable to indanol **19** and dramatically improved over pyridine **20**. Transposing the pyridine nitrogen to the other available aromatic carbon (**22**) resulted in a dramatic loss in binding affinity. Examination of the impact of indane fluorination

confirmed expected potency trends [26, 28]: **23** without any fluorination showed a significant loss in potency, while use of the cis-vicinal difluoro moiety in **24** afforded a slight increase in potency over **21**. Crystallization of **23** indicated a tyrosine phenol to arene contact which was similar to trifluoromethyl benzene **18**.

Table 4 Crystal structures of 23 and 26

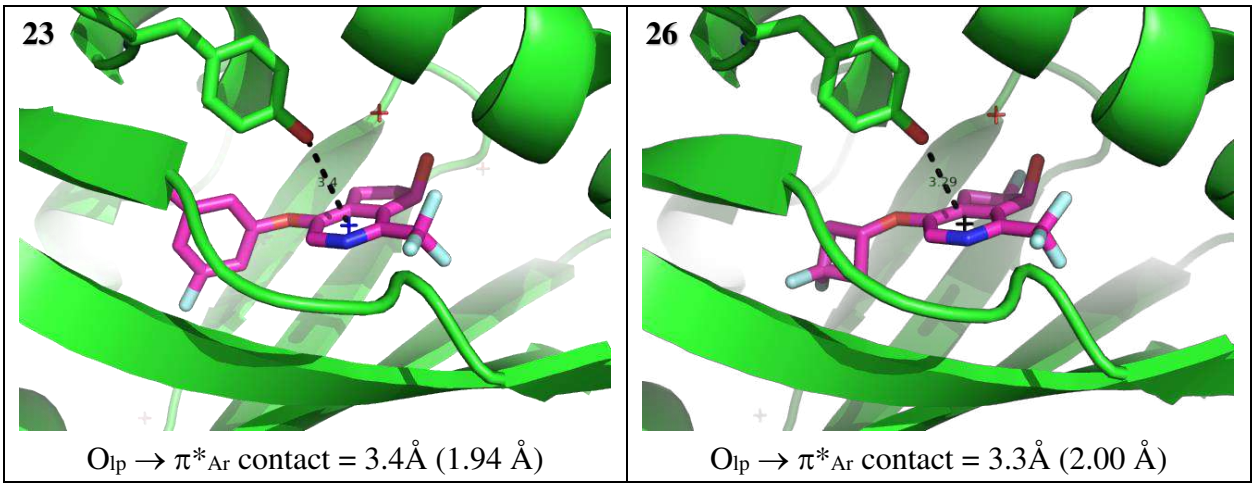

$O_{lp} \rightarrow \pi^*_{Ar}$ contact = 3.4Å (1.94 Å) | $O_{lp} \rightarrow \pi^*_{Ar}$ contact = 3.3Å (2.00 Å)

A panel of crystal structures of **23** (PDB code **6X37**) and **26** (PDB code **6X3D**) in complex with the HIF-2α PAS-B*/ARNT PAS-B* dimer showing the relevant distance between the oxygen of Tyr281 and the arene centroid (black). The resolution of each crystal structure is shown in parenthesis after the contact distance.

Our discovery of the trifluoromethyl pyridine as an appealing replacement of the trifluoromethyl benzene (CLogP = 3.92 for R_1 = 3-CN-5-F-C_6H_3, R_2 = CF_3, A = CH, B = CH, X = H, Y= F in Table 3) with better predicted physical properties presented us with the opportunity to explore our best aliphatic replacements of the benzonitrile (Table 1) in combination with this new core. Substituting the benzonitrile of **21** with 3,3-difluorocyclobutane, the most potent aliphatic replacement identified, afforded **26** whose activity was comparable to **21**. Cis-vicinal difluorination of the 3,3-difluorocyclobutane derivative (**27**), however, resulted in a more modest improvement in potency compared to the benzonitrile derivative **24**. Crystallization of **26** revealed a short contact between the phenolic oxygen and arene surface of the pyridine (3.3Å)

which was similar to that observed with trifluoromethyl sulfone derivative **12**. Lastly, the importance of the trifluoromethyl group was evaluated. Consistent with our notion of a putative $O_{lp} \rightarrow \pi^*_{Ar}$ interaction being important for binding, the difluoromethyl derivative **28**, being less electron deficient, experienced a loss in binding affinity (>200 fold).[7]

Evaluation in vivo and in vitro

24 and **27**, the 2 most promising leads, were evaluated in our pharmacokinetic/pharmacodynamic (PK/PD) model (Fig. 3) to quickly ascertain whether they presented compelling alternatives to our indanol based HIF-2α antagonists. Mice were grown with 786-O xenografts to an average tumor volume of ~250 mm^3, and then treated BID over a period of 60 h with doses of **24** and **27** at 3 mg/kg and PT2385 at 10 mg/kg as control. After 72 h, plasma was drawn to determine exposure (PK), and the excised tumors were analyzed for PD effect by evaluation of expression of HIF-2α target genes VEGFA and cyclin D1 (CCND1). As shown in Fig. 3, both **24** and **27** performed well in the PK/PD experiment with inhibition of gene transcription similar to PT2385 and greater plasma exposure at a lower dose.

[7] The change in pyridine pKa on switching from $-CF_3$ to $-CF_2H$ probably contributes to the loss in binding affinity and helps explain the magnitude of that loss. Similar point changes in fluorination have had impacts ranging from 2-15x in related indane systems.

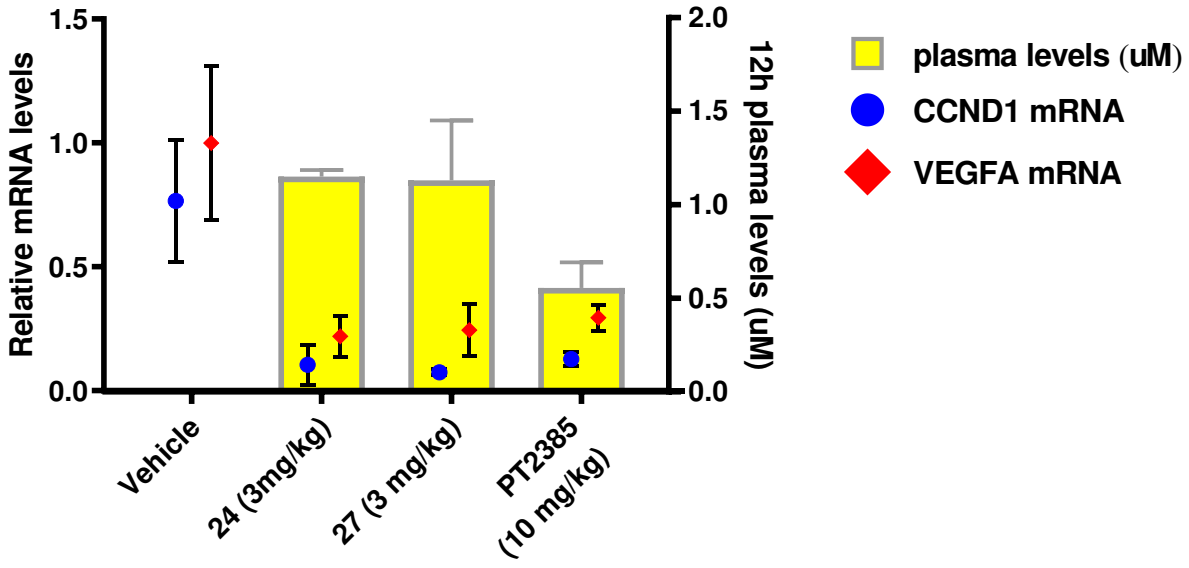

Fig. 3 PK/PD evaluation of **24**, **27**, and PT2385 in 786-O mouse xenograft (female SCID/beige mice, n = 3, dosed at 3 or 10 mg/kg po, b.i.d., for 3 days to achieve steady-state exposure). Compounds were formulated with 10% absolute ethanol, 30% PEG400, 60% water containing 0.5% methylcellulose and 0.5% Tween80®. Tumors were harvested 12 h after administration of the final dose, and total RNA was isolated from the tumor samples and used to make single-stranded cDNA. The resulting cDNA was used in quantitative polymerase chain reactions (qPCR); mRNA levels were normalized to internal control cyclophilin B mRNA levels in each sample.

Encouraged by these results we elected to profile **24** and **27** further in vitro (Table 5). The plasma protein binding data generated in human and mouse indicated that **24** and **27** were comparable to PT2385 in human, but more free in the mouse. Permeability was compared across MDCK-MDR1 and both **24** and **27** showed good permeability that was similar in performance to PT2385. Most gratifying were solubility measurements which showed, as predicted by prior precedent [33, 34], that incorporation of heterocycles into the indane scaffold and increasing the Fsp^3 improved solubility. Trifluoromethyl pyridine **24** was 8-fold more soluble than PT2385. Furthermore, replacement of the benzonitrile in **24** with the 3,3-difluorocyclobutane (**27**) resulted in an additional 3-fold improvement in solubility. Rounding out the in vitro analysis were stability measurements in microsomes which suggested good stability for **24** and **27**.

Table 5 Select in vitro parameters for **PT2385**, **24**, and **27**

Compound	PT2385	24	27
Luciferase EC_{50} (nM)	27	7.8	10
VEGFA EC_{50} (nM)	46	9.3	21
PPB m/h (%)	71/82	58/76	55/78
Human free fraction adjusted EC_{50} (nM)	150	33	45
12h plasma concentration (μM)	0.55	1.15	1.13
Papp A→B (nm/s)	70.2	65.4	78.9
B→A/A→B ratio	0.63	0.7	0.6
Thermodynamic solubility (μg/mL) (pH 7.4)	23	179	579
CL_{int} m (mL/min/kg)	19.9	12	< 12
CL_{int} h (mL/min/kg)	4.7	4	< 3
CL_{int} rat (mL/min/kg)	22.6	17.5	< 6
Hepatocyte ER dog	52	52	66

Based on results from the PK/PD and in vitro screenings, **24** and **27** were advanced into rat and dog PK. As indicated in Table 6, **24** and **27** demonstrated reasonable clearance and good bioavailability and exposure. Importantly, the improved solubility of **24** and **27** enabled achievement of good oral exposure after dosing with the methyl cellulose-tween (MCT) formulation in dog.[8]

However, while rat and dog PK were important milestones to overcome, in order to progress with a high likelihood of improvement over PT2385, **24** and **27** needed to demonstrate low susceptibility to glucuronidation. To ascertain the level of glucuronide formation, plasma samples from dog PK were evaluated for the initial level of parent, then incubated with β-

[8] The bioavailability for **24** and **27** contrasts favorably with that observed for PT2385 (%F = 25) in the MCT only formulation. 10 mg/kg oral dose of PT2385 (suspension in 0.5% methylcellulose, 0.5% Tween 80 in water) in male beagles (n = 3).

glucuronidase to hydrolyze any glucuronide to parent, and finally evaluated for total parent concentration. The difference between total parent and initial parent determined the amount of glucuronide that had formed. Prior experiments indicated that the cis-vicinal difluoride in PT2977 improved the AUC ratio of glucuronide metabolite to parent from 1.8 (in the case PT2385) to 0.24 [28]. However, the AUC ratios of glucuronide metabolite to parent were similar to or worse than PT2385 for **24** (1.6) and **27** (3.3). UGT profiling confirmed that, like PT2385, UGT 2B17 was the primary UGT for glucuronidation of both trifluoromethyl pyridine analogs (Fig. 4). Finally, *in vitro* profiling of **24** and **27** in dog hepatocytes (Table 5) indicated that the performance of **24** and **27** was similar to or worse than PT2385. Collectively, the body of data around glucuronidation and phase 2 metabolism of **24** and **27** suggested that neither compound would be a suitable replacement. This result was surprising considering that **24** and **27** contain the cis-vicinal difluoride which proved consequential in alleviating glucuronidation for PT2977. It appears that the trifluoromethyl pyridine may impart increased acidity[9] to the alcohol moiety which overcomes the beneficial effect of the cis-vicinal difluoride. As the glucuronidation is an S_N2 reaction, increased acidity at the alcohol would prove deleterious by enhancing alcohol nucleophilicity [38]. As a result of their marginal glucuronidation profiles, **24** and **27** were not advanced further.

Table 6 Rat and dog PK parameters for **24** and **27**

Species	Compound	CL (mL/min/kg)	AUC_{0-t} (hr*μM)	V_{SS} (L/kg)	$t_{1/2}$ (h)	%F
	24	33[a]	5.8[b]	1.7[a]	0.92[a]	44[b]

[9] The pKa in DMSO reported for diphenylmethane ($PhCH_2Ph$) and 3-benzylpyridine (3-$PhCH_2$-pyridine) are 32.2 and 30.1, respectively. See: Ripin, D.H.; Evans, D.A. Evans pKa Table. http://ccc.chem.pitt.edu/wipf/MechOMs/evans_pKa_table.pdf (accessed December 24, 2020).

Rat	**27**	3.0[a]	96.0[b]	5.1[a]	26.6[a]	86[b]
Dog	**24**	14.7[c]	12.1[d]	6.4[c]	8.3[c]	86[d]
	27	17.1[c]	7.8[e]	2.77[c]	5.2[c]	60[e]
	24-glucuronide	ND	19.5[d]	ND	7.2[c]	ND
	27-glucuronide	ND	26.6[e]	ND	6.5[c]	ND

[a] 1 mg/kg intravenous dose (solution in 10% dimethylacetamide, 10% EtOH, 40% PEG400, 40% water) in male Sprague-Dawley rats (n = 3). [b] 10 mg/kg oral dose (suspension in 10% EtOH, 30% PEG400, 60% (0.5% methylcellulose, 0.5% Tween 80 (aq)) in male Sprague-Dawley rats (n = 3). [c] 1 mg/kg intravenous dose (solution in 20% EtOH, 40% PEG400, 40% water) in male beagles (n = 3). [d] 5 mg/kg oral dose (suspension in 0.5% methylcellulose, 0.5% Tween 80 in water) in male beagles (n = 3). [e] 5 mg/kg oral dose (suspension in 0.5% methylcellulose, 0.1% Tween 80 in water) in male beagles (n = 3).

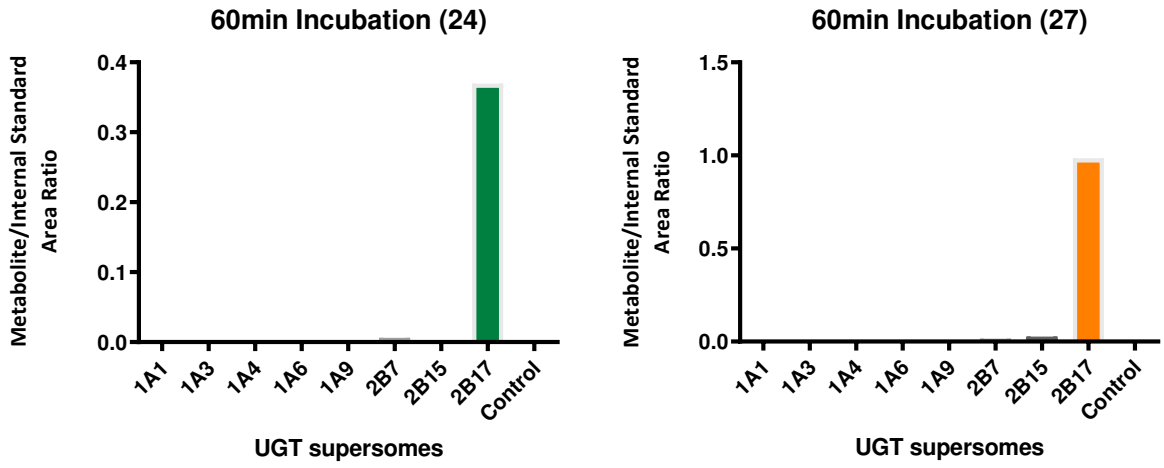

Fig. 4 Glucuronide formation of **24** and **27** by recombinant human UGTs

Calculations examining the $O_{lp} \rightarrow \pi^*_{Ar}$ contribution to binding

Calculations of the $O_{lp} \rightarrow \pi^*_{Ar}$ interaction of our HIF-2α antagonists enabled a retrospective analysis that confirmed our intuitive suspicion of their importance. Highlighted in Fig. 5a is a breakdown of the energetics which makeup the interaction between **12** and Tyr281. Using the metrical parameters determined from the crystal structure of **12**, energetic contributions were calculated using MP2/6-311++G(d,p) theory for 3 different interactions: (1) the Tyr281 $O_{lp} \rightarrow \pi^*_{Ar}$ ~9.2 kcal/mol, (2) the Tyr281 H-bond donation to water ~4.7 kcal/mol, and (3) the water H-bond donation to the indanol oxygen ~10.3 kcal/mol. Interestingly, the interaction of the tyrosine with water (2) contributes the least to binding. The remaining interactions are both twice the amount of the tyrosine-water (2) interaction and suggest that modulation of these interactions may be more valuable. While utilizing a lone pair-pi interaction for drug design is unconventional, the barriers to take advantage of it are low: changing the π^*_{Ar} of a small molecule is well within the capacity of medicinal chemists.

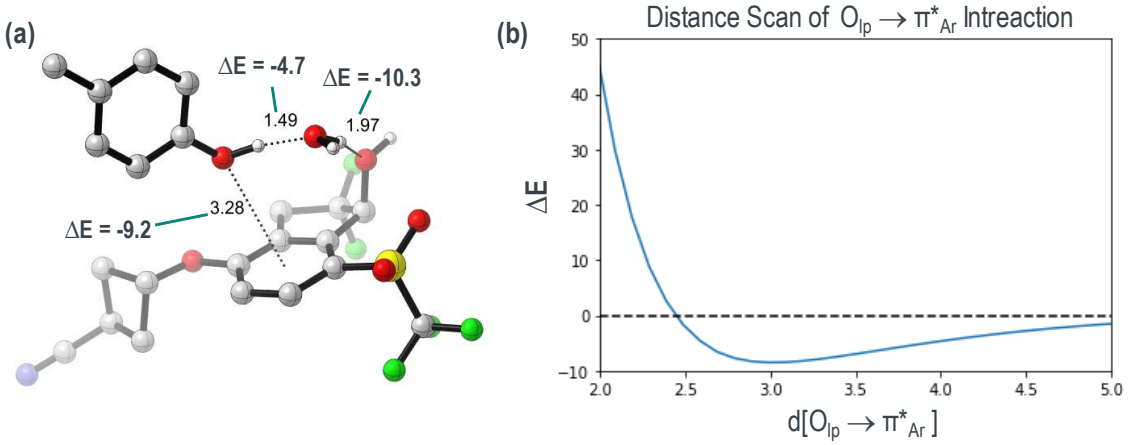

Fig. 5 (a) Calculated interaction energies for **12** based on the metrical parameters derived from the crystal structure **6X2H**. Distance listed in Å and energy in kcal/mol. (b) Scan of the impact of distance on the energy of the $O_{lp} \rightarrow \pi^*_{Ar}$ interaction (distance varied between the oxygen and aromatic center, angle $O_{lp} \rightarrow \pi^*_{Ar}$ is fixed to be 83.8º). Both calculations use MP2/6-311++G(d,p) theory.

Before analyzing the impact of the π^*_{Ar} on the $O_{lp} \rightarrow \pi^*_{Ar}$ interaction in greater detail, we sought to better understand the contribution of the O_{lp}. A scan of the energy of interaction with the arene was conducted by varying the distance (Fig. 5b). As expected, there was an increased energy of interaction as the distance from the O_{lp} to the arene decreased, achieving a maximum calculated interaction at 2.9-3.0 Å. Below this value, decreasing the $O_{lp} \rightarrow \pi^*_{Ar}$ distance proved deleterious with repulsive forces outweighing interactive ones. The angle of interaction is also important, but it was beyond the scope of our study. It is sufficient to say that the ideal angle of interaction for the $O_{lp} \rightarrow \pi^*_{Ar}$ ranges is ~83 degrees and is satisfactory for the molecules analyzed here (see Fig. 6 for angles of interaction). The geometric parameters for the lone pair-pi interaction are similar to the water aromatic system as illustrated in Jain, et al [39].

A key question in furthering our retrospective analysis of the $O_{lp} \rightarrow \pi^*_{Ar}$ interaction was to resolve the discrepancy between the potencies observed for the $-CF_3$ and $-SO_2Me$ groups and their electron withdrawing potential (σ_p = 0.54 and 0.72, respectively). Using the metrical parameters generated from our crystal structures (**26**, **12**, and **5TBM**), we generated a simplified set of indane analogs where the aryloxy or alkoxy group was replaced with a methoxy (Fig. 6). Calculating the interaction potential across the simplified arenes recapitulated the observed potency trends. Surprisingly, the calculations showed that $-CF_3$ pyridine is like the $-CF_3$ benzene in $O_{lp} \rightarrow \pi^*_{Ar}$ interaction potential. This result suggests that for the pyridine derivatives the balance between $O_{lp} \rightarrow \pi^*_{Ar}$ distance and pyridine nitrogen pKa is most important for potency (compare **19** vs **21**, and **26** vs **28**) rather than increased π^*_{Ar} potential. As expected, for the remaining analogs, the $-SO_2CF_3$ group shows the strongest interaction potential. The $-SO_2Me$ group has the smallest calculated interaction potential, yet by its inductive effect it should be superior to $-CF_3$. Calculation of the electrostatic potential (ESP) surface for indanols with -

SO_2CF_3, -SO_2Me, and -CF_3 groups corroborates that the -CF_3 has the smallest π^*_{Ar} potential (see supplementary information for surface potential maps). It appears that the metrical advantages of the -CF_3 group (closer $O_{lp} \rightarrow \pi^*_{Ar}$ contact, better angle) overcome the smaller π^*_{Ar} potential. Finally, it is interesting to note that the incorporation of the hydroxyl group leads to an enhancement of the $O_{lp} \rightarrow \pi^*_{Ar}$ interaction, likely reflecting an inductive effect of the hydroxyl group on the π^*_{Ar}. Collectively, the results from our calculations support and reinforce the intuitive model of maximizing the hypothesized $O_{lp} \rightarrow \pi^*_{Ar}$ interaction we initially used to drive our structure based drug design efforts: by increasing the π^*_{Ar} and/or decreasing the $O_{lp} \rightarrow \pi^*_{Ar}$ contact improved binding was achieved.

(a)

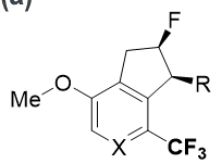

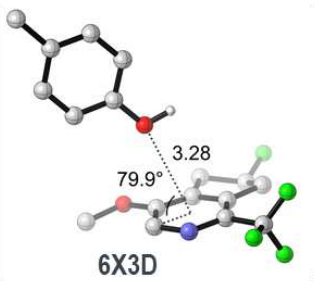

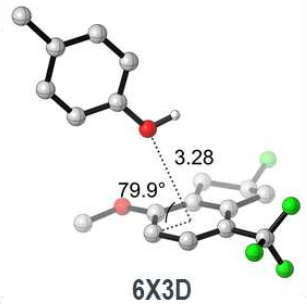

Crystal Structure:	6X3D	6X3D
X/R	N	C-H
H	-5.7	-5.6
OH	-7.3	-7.2

(b)

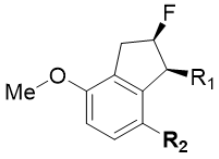

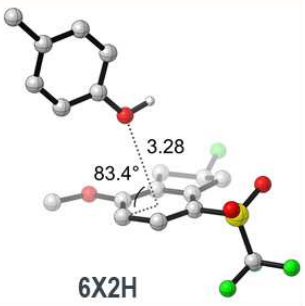

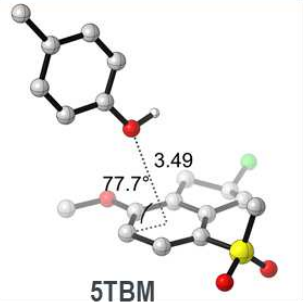

Crystal Structure:	6X2H	5TBM
R_1/R_2	SO_2CF_3	SO_2Me
H	-6.2	-4.1
OH	-7.9	-5.1

Fig. 6 Calculated $O_{lp} \rightarrow \pi^*_{Ar}$ interaction energies for simplified methoxy substituted indane analogs where the electron withdrawing group is trifluoromethyl (a) or sulfone (b). Shown is the modeled interaction, chemical structure and energies of interaction. The crystal structure on which the angle and distance of interaction are based is listed in the final row. All calculations performed at MP2/6-311++G(d,p) level of theory.

Chemical synthesis

Synthesis of the initial library screening replacements of the benzonitrile moiety with aliphatic groups to increase the Fsp^3 began with the $Me_3SiOSO_2CF_3$ catalyzed ketalization of ketone **29** to **30** (Scheme 1).[10] Exposure of fluoro arene **30** to PMBOH under basic conditions results in efficient S_{NAr} to afford the PMB protected phenol intermediate which is then deketalized by PPTS catalyzed deprotection to yield ketone **31**. Difluorination of the ketone **31** was achieved by *in situ* formation of the 3-methoxypropyl imine and subsequent treatment with F-TEDA-BF_4 followed by imine hydrolysis. Enantioselective reduction of the intermediate difluoroketone to indanol **32** was completed by Noyori Ruthenium catalyzed transfer hydrogenation.[11] To yield an intermediate capable of rapidly screening aliphatic replacements of the benzonitrile, we elected to use a Mitsunobu reaction to install the aliphatic piece on an advanced phenol. As such, it was necessary to perform protecting group manipulations on indanol **32**. First, a TBS protecting group was introduced onto the indanol by use of $tBuMe_2SiOSO_2CF_3$. Gratifyingly, the resulting doubly protected intermediate could have the PMB group selectively removed by treatment with TFA to afford phenol **33**. In one pot, phenol **33** could be rapidly transformed to the final products (**1**-**13**) by sequential Mitsunobu reaction to install the aliphatic group followed by buffered TBAF mediated deprotection of the TBS protected indanol.

[10] Previously described as intermediate **31g** in reference 26. Likewise, the ketone with the methyl sulfone was described as **31i**.
[11] In some early examples, racemic indanol was generated by reduction $NaBH_4$ in MeOH.

Scheme 1 General synthesis of **1-13**[a]

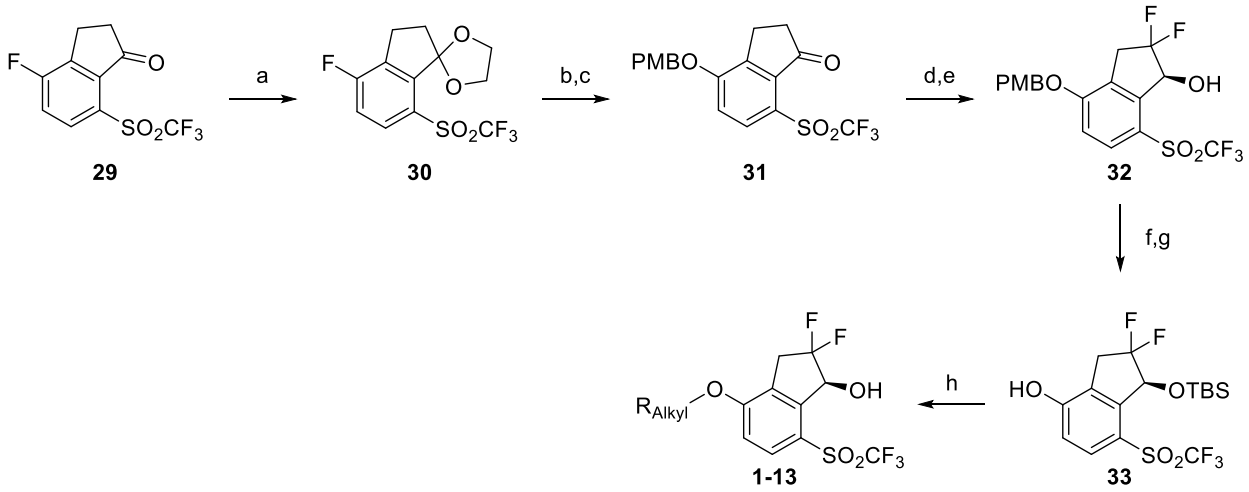

[a]Reagents and conditions: (a) $(Me_3SiOCH_2)_2$, $Me_3SiOSO_2CF_3$, CH_2Cl_2, -78 °C → rt, 80%; (b) PMBOH, KOH, CH_3CN, 25 °C, 79%; (c) PPTS, H_2O/acetone, 80 °C; (d) Me_3CCO_2H, 3-methoxypropylamine, cyclohexane/toluene, 104 °C, then Na_2SO_4, F-TEDA-BF_4, CH_3CN, 60 °C, then aq HCl, 50%; (e) [(*R*,*R*)-Ts-DPEN]RuCl(*p*-cymene), HCO_2H, Et_3N, CH_2Cl_2, 4 °C, 71%; (f) 2,6-lutidine, $tBuMe_2SiOSO_2CF_3$, -78 °C → rt, 99%; (g) 1:1 TFA/CH_2Cl_2, rt, 89%; (h) $R_{Alkyl}OH$, PPh_3, DIAD, rt, overnight, then AcOH, TBAF, 60 °C, variable yield (40% for **6**).

Preparation of the trifluoromethyl comparator **14** utilized phenol indanone **34** (Scheme 2). A sequence of Mitsunobu alkylation of the phenol, aromatic ring iodination mediated by F-TEDA-BF_4 activation of elemental iodine [40], and ketone difluorination produced intermediate **35**. Elaboration to **14** was achieved by *in situ* generation of a trifluoromethyl copper species for replacement of the iodo moiety followed by enantioselective ketone reduction mediated by Noyori ruthenium catalyzed transfer hydrogenation.

Scheme 2 General synthesis of **14**[a]

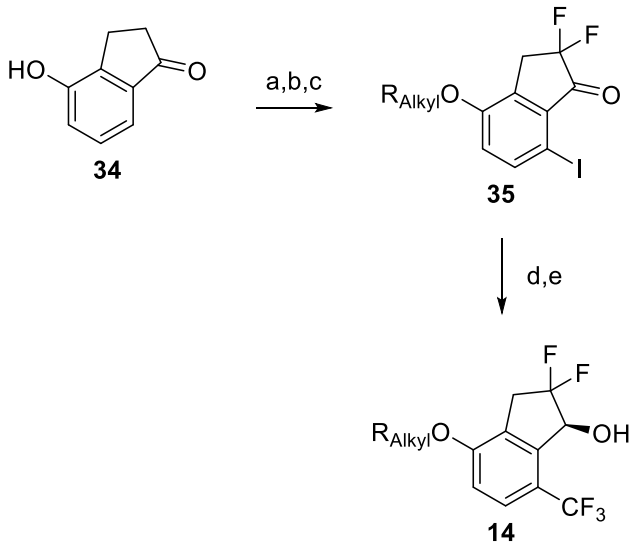

[a]Reagents and conditions: (a) $R_{Alkyl}OH$, PPh_3, DIAD, PPh_3, 0 → 50 °C, 85%; (b) F-TEDA-BF_4, I_2, CH_3CN, 0 → 25 °C, 68%; (c) Me_3CCO_2H, 3-methoxypropylamine, cyclohexane/toluene, 104 °C, then Na_2SO_4, F-TEDA-BF_4, CH_3CN, 70 °C, then aq HCl, 32%; (d) $FSO_2CF_2CO_2Me$, CuI, DMF, 100 °C, 99%; (e) [(*R*,*R*)-Ts-DPEN]RuCl(*p*-cymene), HCO_2H, Et_3N, CH_2Cl_2, 4 °C, 79%; Note: yields shown are for R_{Alkyl} = 2,2-difluoroethoxy.

The synthesis of examples **15**, **16**, **17**, and **19** were previously described [26]. **18** was prepared starting from indanone **36** following a sequence of copper mediated trifluoromethylation of the bromide, Noyori ruthenium catalyzed enantioselective ketone reduction, and S_{NAr} displacement of the aryl fluoride with 3,5-difluorophenol (Scheme 3). In contrast to iodide **35** and trifluoromethyl sulfone **30**, yields for the trifluormethylation and S_{NAr} reactions en route to **18** were significantly worse. These results likely reflect the inferior reactivity of the bromide in copper mediated trifluoromethylation of aryl halides and the reduced electron withdrawing potential of the trifluoromethyl group to enhance S_{NAr} reactivity.

Scheme 3 Synthesis of **18**[a]

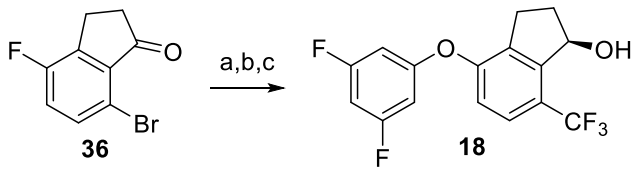

[a]Reagents and conditions: (a) $FSO_2CF_2CO_2Me$, CuI, DMF, 100 °C, 22%; (b) [(*R*,*R*)-Ts-DPEN]RuCl(*p*-cymene), HCO_2H, Et_3N, CH_2Cl_2, rt, 80%; (c) 3,5-difluorophenol, Cs_2CO_3, DMF, 135 °C, 8%.

The 2-fluoro-5-bromo nicotinic acid **37** formed the basis for the synthesis of **20** (Scheme 4). S_{NAr} of the fluoride with thiomethoxide installed the thiomethyl group in high yield. This step was followed by directed lithiation of the pyridine with LiTMP and quenching with DMF to afford an intermediate aldehyde which was subjected to the Horner-Wadsworth-Emmons (HWE) reaction to give acrylate **38**. Cobalt mediated reduction of the olefin in **38** spared the bromide and set the stage for cyclization to the azaindanone. LHMDS induced ring closure followed by hydrolysis/decarboxylation at high temperature produced an azaindanone intermediate which was exposed to oxone to mediate oxidation of the sulfide to sulfone **39**. To replace the bromide with a hydroxyl group, it was necessary to protect the ketone as a ketal. Palladium catalyzed hydroxylation [41] of the ketal bromide cleanly afforded hydroxy pyridine **40**. Use of mixed diaryl iodonium tosylates derived from anisole enabled selective arylation of the hydroxyl group. Then ketal deprotection with perchloric acid gave ketone **41**. Elaboration to **20** was realized by formation of the TBS enol ether, followed by oxidation with F-TEDA-BF_4 and dynamic kinetic resolution of the intermediate fluoroketone by ruthenium-catalyzed transfer [42].

Scheme 4 Synthesis of **20**[a]

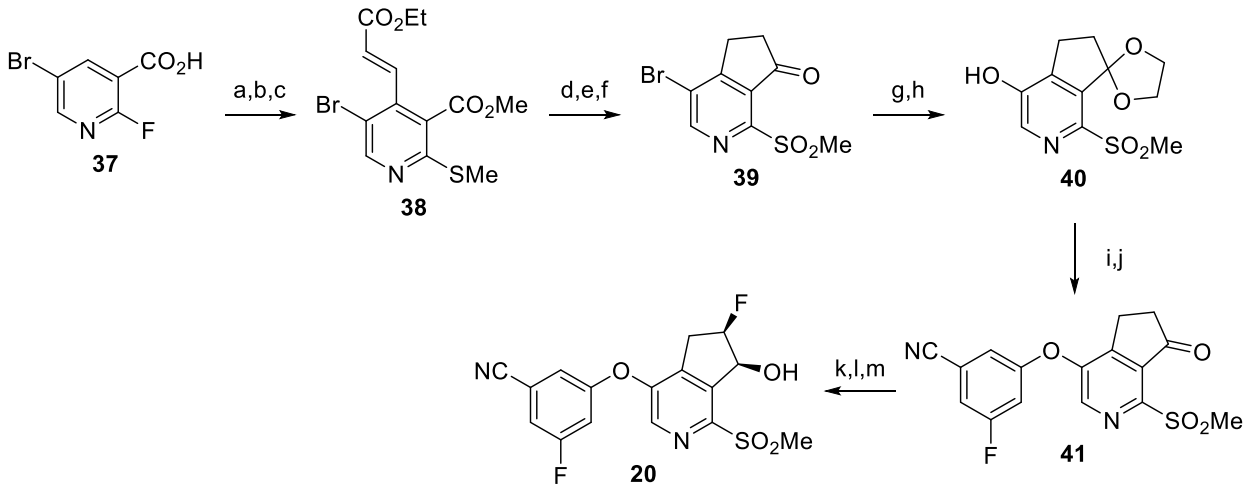

[a]Reagents and conditions: (a) K_2CO_3, NaSMe, DMF, 0 °C → rt, 92%; (b) TMP, nBuLi, DMF, THF, -50 °C; (c) $(EtO)_2POCH_2CO_2Et$, LiCl, DBU, CH_3CN, rt, concentrate, then Me_2SO_4, DMF, rt, 66% over 2 steps; (d) $CoCl_2$, $NaBH_4$, MeOH, 0 °C, 57%; (e) LHMDS, THF, -78 °C, workup, then DMSO/H_2O, 150 0 °C, μW, 92%; (f) $2KHSO_5 \cdot KHSO_4 \cdot K_2SO_4$, MeOH, 0 °C → rt, quant; (g) $(Me_3SiOCH_2)_2$, $Me_3SiOSO_2CF_3$, CH_2Cl_2, 0 °C → rt, 18%; (h) 20 eq H_2O, 3 eq KOH, 2 mol% tBuBrettPhos Pd G3, 2 mol% tBuBrettPhos, THF, 80 °C; (i) Ar_2IOTs, K_2CO_3, CH_3CN, 50 °C, 44% over 2 steps; (j) 70% aq $HClO_4$, CH_2Cl_2, 0 °C → rt; (k) TBSOTf, Et_3N, CH_2Cl_2, 0 °C → rt; (l) F-TEDA-BF_4, CH_3CN, rt, 48% over 3 steps; (m) [(*R*,*R*)-Ts-DPEN]RuCl(*p*-cymene), HCO_2H, Et_3N, CH_2Cl_2, 4 °C, 63%;

The synthesis of **21** began with the innate C-H trifluoromethylation [43] of pyridine **42** to afford a separable mixture of isomers slightly favoring the desired product **43** (Scheme 5). A sequence of ketalization and palladium catalyzed hydroxylation [41] served to transform ketone **43** into hydroxy pyridine **44**. Hydroxyl group arylation to produce diaryl ether **45** was achieved via the mixed diaryl iodonium tosylates used in Scheme 4 except that solvent was switched to THF. Perchloric acid served to remove the ketal and generate ketone **46**. Finally, the sequence of enolization, fluorination, and enantioselective reduction outlined in the final 3 steps of Scheme 4 served to generate **21**. By treatment with sodium borohydride, intermediate **46** also enabled the synthesis of the racemic non-fluorinated azaindanol derivative **23**.

Scheme 5 Synthesis of **21** and **23**[a]

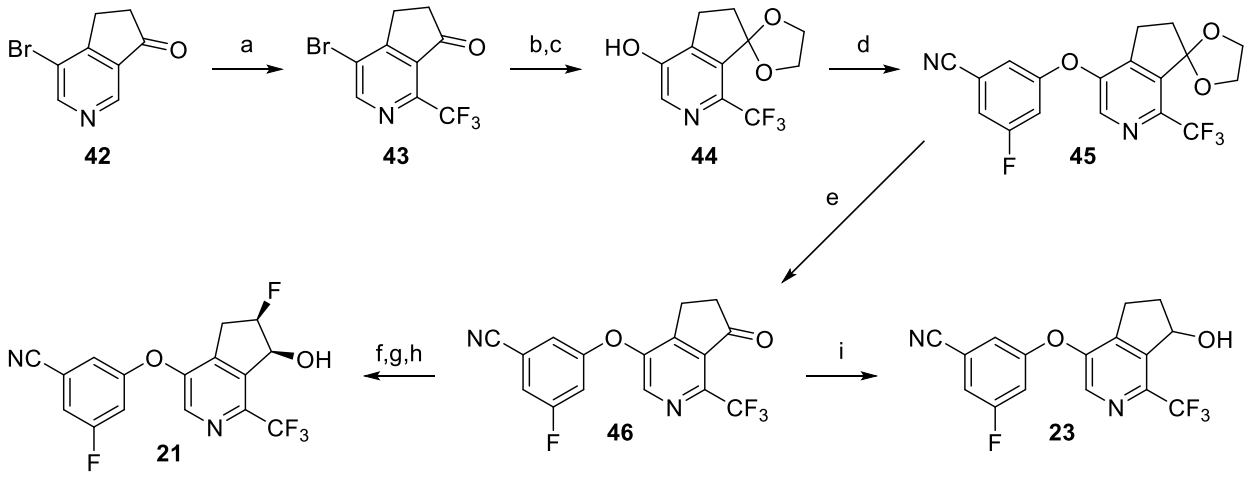

[a]Reagents and conditions: (a) $(CF_3SO_2)_2Zn$, tBuOOH, H_2O/CH_2Cl_2, 0 °C → rt, 30%; (b) $(Me_3SiOCH_2)_2$, $Me_3SiOSO_2CF_3$, CH_2Cl_2, 0 °C → rt, 58%; (c) 20 eq H_2O, 3 eq KOH, 2 mol% tBuBrettPhos Pd G3, 2 mol% tBuBrettPhos, THF, 80 °C; (d) Ar_2IOTs, K_2CO_3, THF, 0 °C → 40 °C, 48%; (e) 70% aq $HClO_4$, CH_2Cl_2, 0 °C; (f) TBSOTf, Et_3N, CH_2Cl_2, 0 °C → rt; (g) F-TEDA-BF_4, CH_3CN, rt, 97% over 3 steps; (h) [(*R*,*R*)-Ts-DPEN]RuCl(*p*-cymene), HCO_2H, Et_3N, CH_2Cl_2, 4 °C, 77%; (i) $NaBH_4$, MeOH, 0 °C, 88%.

Preparation of the regioisomeric trifluoromethyl pyridine **22** utilized nicotinaldehyde **47**. A sequence of HWE olefination, cyanide cross-coupling at the iodo group, and hydrogenation of the olefin transformed **47** into nitrile **48**. LHMDS mediated cyclization of the ester in **48** onto the nitrile generated a vinylogous carbamate intermediate that could be triply hydrolyzed and decarboxylated under acidic conditions to generate pyridone **49**.[12] Exposure of pyridone **49** to ketalization conditions afforded an inseparable 1:1 mixture of enol ether **50** and the ketal. Despite the poor selectivity for ketalization, the enol ether provided the opportunity to effect a tandem fluorination-ketalization sequence. Treatment of **50** with F-TEDA-BF_4 yielded the expected fluoro ketal **51**, which was subsequently transformed to diaryl ether **52** by sequential iodination with NIS, arylation with a mixed diaryliodonium tosylate, and ketal deprotection with perchloric acid. Generation of a copper trifluoromethyl intermediate by decomposition of diphenyl thioether salts with elemental copper enabled replacement of the iodo group with

[12] Hydrolysis includes of the ester, fluoride, and amino group of the vinylogous carbamate.

trifluoromethyl. Finally, racemic diastereoselective reduction of the ketone by sodium borohydride enabled the completion of **22**.

Scheme 6 Synthesis of **22**[a]

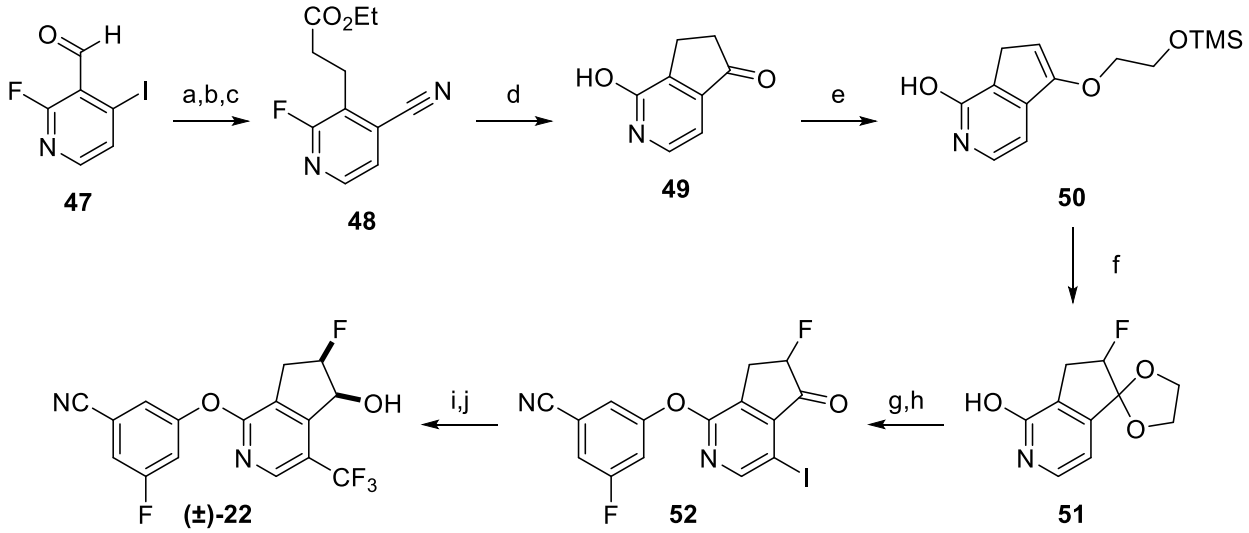

[a]Reagents and conditions: (a) $(EtO)_2POCH_2CO_2Et$, LiCl, DBU, CH_3CN, rt, 86%; (b) $Zn(CN)_2$, $Pd_2(dba)_3$, dppf, DMA, 110 °C, 97%; (c) 10% Pd/C, 1 atm H_2, MeOH, rt, 68%; (d) LHMDS, THF, -78 °C, workup with aq NH_4Cl, then aq H_2SO_4, dioxane, 120 °C, μW, 65%; (e) $(Me_3SiOCH_2)_2$, $Me_3SiOSO_2CF_3$, CH_2Cl_2, 0 °C → rt; (f) F-TEDA-BF_4, CH_3CN, rt, 56%; (g) NIS, CH_3CN, 80 °C, concentrate, then Ar_2IOTs, K_2CO_3, CH_3CN, 80 °C; (h) 70% aq $HClO_4$, CH_2Cl_2, 0 °C → 44 °C; (i) $Ph_2S(CF_3)OTf$, Cu, DMF, 60 °C, 83%; (j) $NaBH_4$, MeOH, 0 °C, 83%.

Installation of the cis-vicinal difluoride in azaindanol **24** was initiated by a stepwise benzylic bromination and silver mediated hydrolysis of ketal **45** to generate alcohol **53** (Scheme 7). Dess-Martin oxidation of the alcohol yielded an intermediate ketone which was transformed into the enol silane and then fluorinated with F-TEDA-BF_4. Dynamic kinetic resolution of the resulting fluoroketone **54** by ruthenium-catalyzed transfer hydrogenation gave excellent selectivity for cis-fluorohydrin **55** [42].[46] In order to establish the cis-vicinal difluoride motif, it was necessary to engage Mitsunobu chemistry to first invert the hydroxyl group and then saponify the intermediate ester. The resulting trans-fluorohydrin **56** yielded the desired cis-vicinal difluoride by treatment with DAST (diethylaminosulfur trifluoride). Surprisingly, the

fluorination was very clean and did not require recourse to cryogenic conditions as our experience with indane based systems had required [28]. We suspect this result may be due to the inability of the trifluoromethyl pyridines to stabilize a benzylic cation intermediate. Lastly, the ketal was removed by exposure to aqueous perchloric acid and the intermediate ketone was quickly reduced selectively to **24** by treatment with sodium borohydride.

Scheme 7 Synthesis of **24**[a]

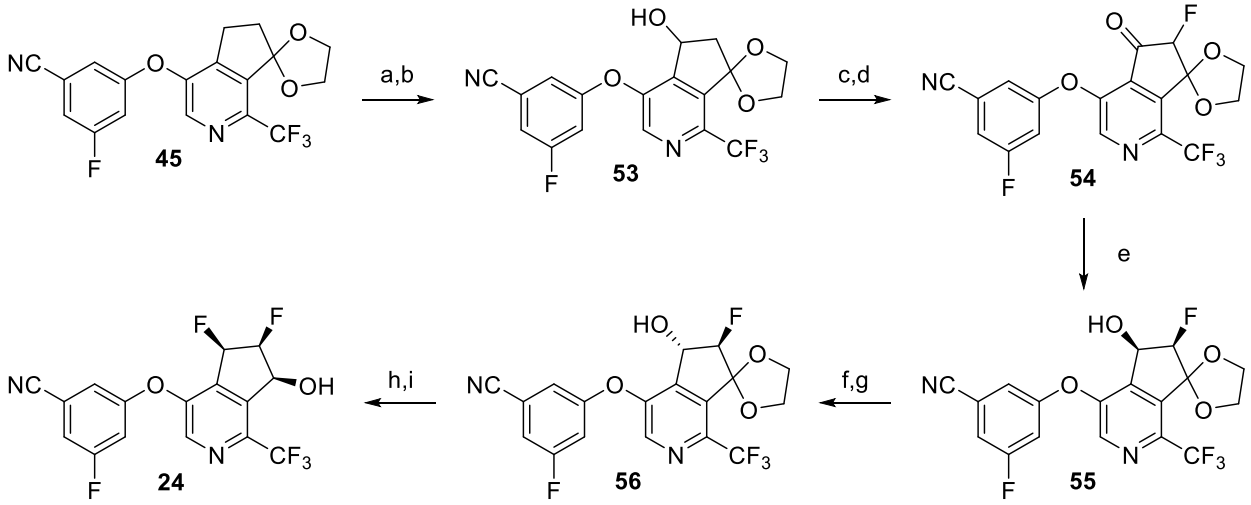

[a]Reagents and conditions: (a) NBS, AIBN, $NaHCO_3$, 1,2-dichloroethane, 80 °C, 51%; (b) Ag_2CO_3, 3:1 1,2-dimethoxyethane/H_2O, 85 °C, 37%; (c) Dess-Martin periodinane, CH_2Cl_2, rt; (d) $tBuMe_2SiOSO_2CF_3$, Et_3N, CH_2Cl_2, 0 °C → rt, aqueous workup, then F-TEDA-BF_4, CH_3CN, rt, 67% over 2 steps; (e) [(*S*,*S*)-Ts-DPEN]RuCl(*p*-cymene), HCO_2H, Et_3N, CH_2Cl_2, 4 °C, 97%; (f) DIAD, PPh_3, 4-$NO_2C_6H_4CO_2H$, THF, rt, 81%; (g) LiOH, THF/H_2O, rt, 78%; (h) DAST, CH_2Cl_2, rt, 67%; (i) 70% aq $HClO_4$, CH_2Cl_2, 0 °C → 44 °C, workup with aq $NaHCO_3$ at 0 °C, then $NaBH_4$, MeOH, 0 °C, 72%.

A byproduct from the ketalization of **43** was enol ether **57** which was used in the construction of **25** and **26** (Scheme 8). Tandem fluoro-ketalization of the enol ether was induced by treatment with F-TEDA-BF_4. Subsequent palladium catalyzed hydrolysis of the bromide enabled installation of the hydroxyl group in **58**. Interestingly, the hydrodefluorination product **44** was observed as a minor inseparable byproduct of the hydroxylation reaction in a 2:1 ratio. The mixture of hydroxylated ketals was moved forward by a sequence of Mitsunobu alkylation

of the hydroxyl group, ketal deprotection and enantioselective ketone reduction by transfer hydrogenation to produce the azaindanols **25** and **26**.

Scheme 8 Synthesis of **25** and **26**[a]

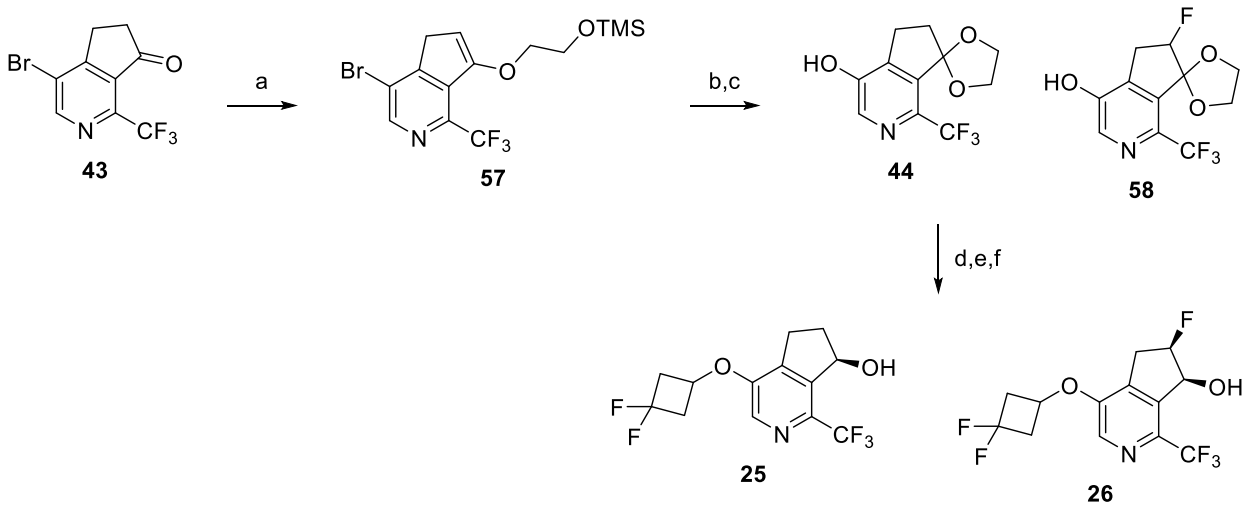

[a]Reagents and conditions: (a) $(Me_3SiOCH_2)_2$, $Me_3SiOSO_2CF_3$, CH_2Cl_2, 0 °C → rt, 31%; (b) F-TEDA-BF_4, CH_3CN, rt, 76%; (c) 20 eq H_2O, 3 eq KOH, 2 mol% tBuBrettPhos Pd G3, 2 mol% tBuBrettPhos, THF, 80 °C; (d) 3,3-difluorocyclobutanol, DIAD, PPh_3, THF, 60 °C, ~67% over 2 steps; (e) 70% aq $HClO_4$, CH_2Cl_2, 0 °C; (f) [(*R*,*R*)-Ts-DPEN]RuCl(*p*-cymene), HCO_2H, Et_3N, CH_2Cl_2, 4 °C, 23% of **25** and 16% of **26**.

The synthesis of **27** began with alkylation of hydroxy pyridine **44** via the alkyl tosylate to install the 3,3-difluorocyclobutane in **60** (Scheme 9). The remaining steps to establish the cis-vicinal difluoride motif of **27** were identical to those outlined in the synthesis of **24** (Scheme 7).

Scheme 9 Synthesis of **27**[a]

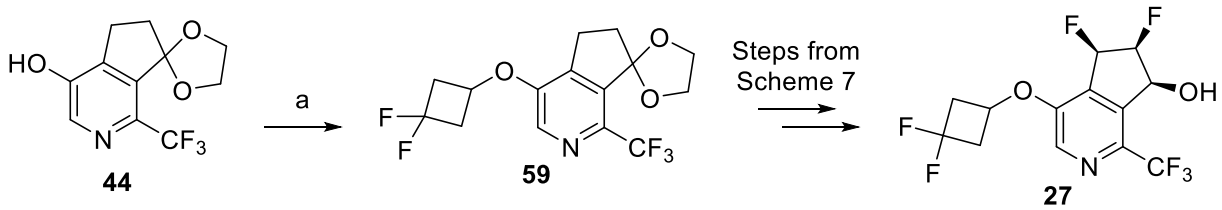

[a]Reagents and conditions: (a) (3,3-difluorocyclobutyl) tosylate, KI, K_2CO_3, CH_3CN, 100 °C, 39%.

Installation of the difluoromethyl group in **28** took advantage of the same innate C-H alkylation chemistry used for trifluoromethylation [43] (Scheme 10). Difluoromethylation of **42** took place in higher yield than the trifluoromethylation to afford ketone **61** which was subsequently reduced and protected to tetrahydropyran acetal **62**. Protection of the hydroxyl group was necessary to effect the direct palladium catalyzed displacement of the bromide by 3,3-difluorocyclobutanol. Despite the improved efficiency of direct displacement with 3,3-difluorocyclobutanol, the low yield contrasted unfavorably with the step wise hydroxylation/alkylation sequence employed by earlier routes. Acetal deprotection followed by oxidation with Dess-Martin periodinane produced ketone **63**. Utilizing the final three steps in the synthesis of **21** (Scheme 5) effected the transformation of **63** into **28**.

Scheme 10 Synthesis of **28**[a]

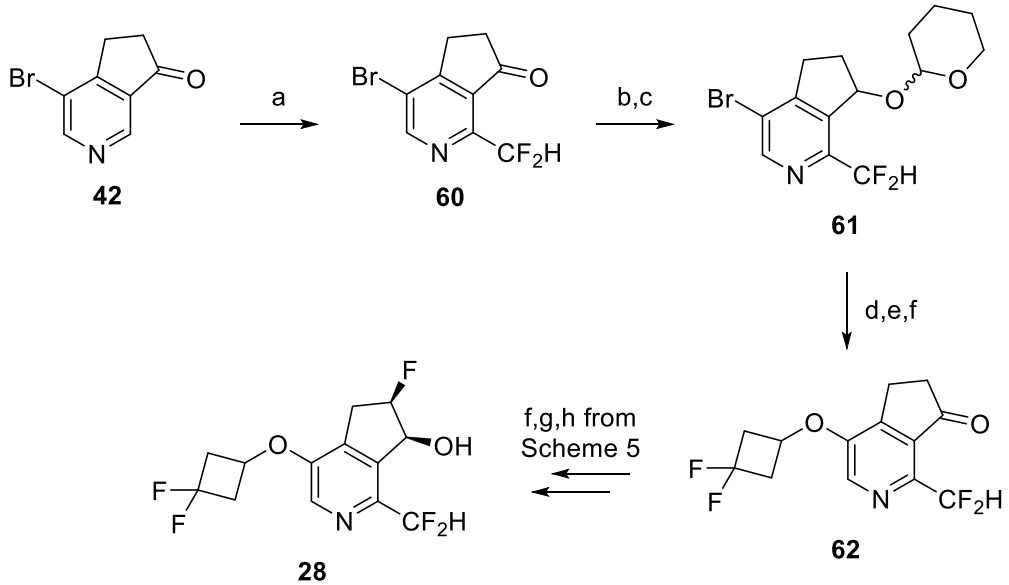

[a]Reagents and conditions: (a) $(CF_2HSO_2)_2Zn$, tBuOOH, H_2O/CH_2Cl_2, 0 °C → rt, 45%; (b) $NaBH_4$, MeOH, 0 °C → rt, 96%; (c) 3,4-dihydropyran, TsOH, CH_2Cl_2, 0 °C → rt, 95%; (d) 3,3-difluorocyclobutanol, Cs_2CO_3, tBuBrettPhos Pd G3, tBuBrettPhos, toluene, 105 °C, 9%; (e) aq HCl, THF, rt; (f) Dess-Martin periodinane, CH_2Cl_2, 0 °C → rt, 52% over 2 steps.

Conclusions

A 3-pronged approach utilizing exploration of increased Fsp^3 , the incorporation of pyridine heterocycles, and the improvement of an $O_{lp} \rightarrow \pi^*_{Ar}$ contact successfully identified novel HIF-2α antagonists with improved physical properties. Essential to our goal of realizing antagonists with improved physical properties was the use of structure-based drug-design to enhance a putative $O_{lp} \rightarrow \pi^*_{Ar}$ interaction. Structures of our earliest analogs with increased Fsp^3 incorporated a trifluoromethyl sulfone which enforced a close $O_{lp} \rightarrow \pi^*_{Ar}$ contact. Subsequent analogs seeking to replace the trifluoromethyl sulfone with a less fluorinated sulfone took a substantial hit in potency. Previous crystal structures helped to rationalize the potency loss by the deterioration of the $O_{lp} \rightarrow \pi^*_{Ar}$ contact. By replacing the sulfone with a trifluoromethyl, a smaller and less electron withdrawing group which maintains an improved $O_{lp} \rightarrow \pi^*_{Ar}$ contact, potency could be restored. While heterocycle incorporation into the indanol proved initially deleterious, by marrying the discovery of the trifluoromethyl group replacement of the sulfone with pyridine integration into the indane, HIF-2α antagonists with suitable potency and superior physical properties could be identified. Further support for the importance of the $O_{lp} \rightarrow \pi^*_{Ar}$ contact came from replacement of the trifluoromethyl group with the less electron withdrawing, nearly isosteric difluoromethyl group and the resulting loss in binding affinity. Finally, retrospective calculations on the $O_{lp} \rightarrow \pi^*_{Ar}$ contact for our HIF-2α antagonists validated the initial design hypothesis and may prove beneficial to other medicinal chemists considering this underutilized interaction for their own discovery efforts. PK/PD experiments predict that trifluoromethyl pyridines **24** and **27** would be superior HIF-2α antagonists to PT2385, however, an evaluation of their glucuronidation potential reveals that they are similar or worse. Despite **24** and **27** not meeting criteria for further advancement, our investigations leading to their discovery

show the power of structure-based drug design to facilitate lead change and highlight the benefit that can result from contemporaneous optimization of multiple parameters.

Experimental

General chemistry considerations

All solvents and reagents were used as obtained. ^{1}H, ^{13}C and ^{19}F NMR of intermediates and exemplified compounds were performed on an Agilent Technologies 400/54 magnet system (operating at 399.85, 101 and 376 MHz, respectively). Vnmrj version 3.2 software pulse sequences were selected from the default experiment set. Chemical shifts are expressed as δ units using trimethylsilane (TMS) as the external standard (in NMR description, s = singlet, d = doublet, t = triplet, q = quartet, m = multiplet, and br = broad peak).

High performance liquid chromatography (HPLC) coupled to a mass spectrometer (MS) was used to determine the purity of the compounds synthesized. The data confirmed that the target compounds had ≥95% of purity. The following analytical method was used to determine chemical purity of final compounds: Agilent 1200 series high performance liquid chromatography (HPLC) system operating in reverse-phase mode coupled to an Agilent 6150 quadrapole spectrometer using an ESI source, water with 0.1% formic acid (mobile phase A), acetonitrile with 0.1% formic acid (mobile phase B), Agilent ZORBAX Eclipse Plus C18, 1.8 μm, 2.1 mm × 50 mm, 40 °C column temperature, 5–95% mobile phase B in 4.0 min, 95% in 2.0 min, 700 μL/min flow rate, UV absorbance detection at 220 and 254 nm. Analyte ions were detected by mass spectrometry in both negative and positive modes (110–800 amu scan range, API-ES ionization).

For some compounds an additional longer method was also used to assay chemical purity: Agilent 1200 series high performance liquid chromatography (HPLC) system operating in reverse-phase mode, water with 0.1% formic acid (mobile phase A), acetonitrile with 0.1% formic acid (mobile phase B), Phenomenex Kinetex 2.6 μm C18 100 Å, 30 mm × 3.0 mm, 40 °C column temperature, 5–95% mobile phase B in 12.0 min, 95% in 2.0 min, 800 μL/min flow rate, UV absorbance detection at 214 and 254 nm.

Routine chromatographic purification was performed using Biotage Isolera One automated systems running Biotage Isolera One 2.0.6 software (Biotage LLC, Charlotte, NC). Flow rates were the default values specified for the particular column in use. Reverse phase chromatography was performed using elution gradients of water and acetonitrile on KP-C18-HS Flash+ columns (Biotage LLC) of various sizes. Normal phase chromatography was performed using elution gradients of various solvents (e.g., hexanes, ethyl acetate, methylene chloride, methanol, acetone, chloroform,

MTBE, etc.). The columns were SNAP cartridges containing KP-SIL (50 μm irregular particles) or SNAP Ultra (25 μm spherical particles) of various sizes (Biotage LLC).

Enantiomeric excess was determined with chiral HPLC. The chiral HPLC analysis was performed on an Agilent Technologies 1200 Series HPLC system. Analytes were detected by UV absorbance at 220 and 254 nm. A detailed description of the analytical method is provided below:

Column: Phenomenex Lux® 5 μm Cellulose-4 5.0 μm 1000 Å, 150×4.60 mm

Flow rate: 1.5 mL/min

Mobile phase A: 0.1% formic acid in water

Mobile phase B: 0.1% formic acid in acetonitrile

Strong needle wash: 90% acetonitrile, 10% water

Weak needle wash: 10% water, 90% acetonitrile

Injection volume: 2 μL.

Column temperature: 40° C.

Autosampler temperature: Room temperature

Run time: 5.0 min

Gradient: 60% mobile phase A and 40% mobile phase B

Details concerning the SPA assay, luciferase assay, VEGFA secretion assay, in vitro microsomal stability assay, plasma protein binding assay, permeability assay, crystallization, in vivo pharmacokinetic experiments, PK/PD study, and in vivo efficacy study were described previously [26].

Animals and ethics approval

The protocols and procedures involving the care and use of animals for this study were reviewed and approved by the Institutional Animal Care and Use Committee (IACUC) of AAALAC-certified animal facilities and the University of Texas Southwestern Medical Center.

Determination of glucuronide levels

Glucuronide analysis of compounds was achieved with the following addition to the bioanalytical protocol previously described [28]:

Material 75mM KPB buffer, pH at 6.8

β-Glucuronidase (G7646-100KU) Lot# 051K8626V

β-Glucuronidase (G7646-100KU) Lot# 051K8626V
Prepare 1mg/ml β-Glucuronidase in 75mM KPB buffer (5319 uints/ml)

1. Add 2.5μL of DMSO to a well in a 96 well plate
2. Add 25μL plasma to the same well in the 96 well plate
3. Add 25μL of 1mg/mL β-Glucuronidase to all the wells including standard curve, QC and samples.
4. Incubate at 37 °C for 20min
5. Add 200μL internal standard.
6. Centrifuge @3000 RPM for 15min
7. Remove 100μL supernatant to anther 96 well plate which contains 100μL H_2O

The final concentration is 0.5mg/mL of β-Glucuronidase in 75mM KPB Buffer, pH at 6.8, incubate at 37 °C for 40min

25 μL plasma from standard curve, QC or study samples is aliquoted to wells in a 96-well plate. 25 μL of 1 mg/mL β-Glucuronidase in 75mM KPB buffer (pH=6.8) is added to each well. After mixing, incubate the samples at 37°C for 20 min, then add 200 μL acetonitrile containing an internal standard. After vortexing, centrifuge the samples at 3000 RPM for 15 min. Transfer 100 μL supernatant to wells in another 96-well plate which contains 100 μL water.

Synthetic Procedures and Characterization Data for 27[13]

(5*R*,6*S*,7*S*)-4-(3,3-difluorocyclobutoxy)-5,6-difluoro-1-(trifluoromethyl)-6,7-dihydro-5*H*-cyclopenta[*c*]pyridin-7-ol (Example 27). *Step A: Preparation of 4-(3,3-difluorocyclobutoxy)-1-(trifluoromethyl)-5,6-dihydrospiro[cyclopenta[c]pyridine-7,2'-[1,3]dioxolane] (**59**).* A solution of 1'-(trifluoromethyl)spiro[1,3-dioxolane-2,7'-5,6-dihydrocyclopenta[c]pyridine]-4'-ol (**44**) (1.90 g, 7.27 mmol), (3,3-difluorocyclobutyl) 4-methylbenzenesulfonate (2.86 g, 10.91 mmol), potassium iodide (1.81 g, 10.91 mmol) and potassium carbonate (2.01 g, 14.55 mmol) in acetonitrile (20 mL) was stirred at 100 °C overnight. The reaction mixture was concentrated to dryness, diluted with ethyl acetate (100 mL), washed with water (100 mL) and brine (20 mL). The organic phase was collected, dried over anhydrous Na_2SO_4, filtered and the filtrate was concentrated. Purification was achieved by chroamtography on silica using 10-20% EtOAc/petroleum ether to afford 4'-(3,3-

[13] Examples **15**, **16**, **17**, and **19** were previously described in reference 26. Full characterization data and procedures for missing compounds is available in the supplementary information.

difluorocyclobutoxy)-1'-(trifluoromethyl)spiro[1,3-dioxolane-2,7'-5,6-dihydrocyclopenta[c]pyridine] as a white solid (1.00 g, 2.85 mmol, 39%). LCMS ESI (+) (M+H) m/z 352. The Mitsunobu reaction can also be used to derivatize the 1'-(trifluoromethyl)spiro[1,3-dioxolane-2,7'-5,6-dihydrocyclopenta[c]pyridine]-4'-ol (**59**).

Step B: Preparation of 5-bromo-4-(3,3-difluorocyclobutoxy)-1-(trifluoromethyl)-5,6-dihydrospiro[cyclopenta[c]pyridine-7,2'-[1,3]dioxolane]. A solution of 4'-(3,3-difluorocyclobutoxy)-1'-(trifluoromethyl)spiro[1,3-dioxolane-2,7'-5,6-dihydrocyclopenta[c]pyridine] (**59**) (1.00 g, 2.85 mmol), 2,2'-azobisisobutyronitrile (93.5 mg, 0.57 mmol), $NaHCO_3$ (420 mg, 5.0 mmol) and 1-bromopyrrolidine-2,5-dione (1.27 g, 7.12 mmol) in 1,2-dichloroethane (20 mL) was sparged with nitrogen for 3 mins. The vessel was sealed and heated to 80 ^oC for 1 h. The reaction mixture was poured into 30 mL of saturated aqueous Na_2SO_3 and extracted with 3 x 30 mL CH_2Cl_2. The combined organics were rinsed with 20 mL of brine, dried with $MgSO_4$, filtered, and concentrated to dryness. Purification was achieved by chromatography on silica using 5-25% EtOAc/hexanes to afford 5'-bromo-4'-(3,3-difluorocyclobutoxy)-1'-(trifluoromethyl)spiro[1,3-dioxolane-2,7'-5,6-dihydrocyclopenta[c]pyridine] as an off-white solid (650 mg, 1.51mmol, 53%). ^1H NMR (400 MHz, $CDCl_3$): δ 8.11 (s, 1H), 5.36-5.31 (m, 1H), 4.98-4.88 (m, 1H), 4.36-4.21 (m, 2H), 4.16-4.07 (m, 2H), 3.26-3.13 (m, 2H), 2.96-2.71 (m, 4H).

Step C: Preparation of 4-(3,3-difluorocyclobutoxy)-1-(trifluoromethyl)-5,6-dihydrospiro[cyclopenta[c]pyridine-7,2'-[1,3]dioxolan]-5-ol. A solution of 5'-bromo-4'-(3,3-difluorocyclobutoxy)-1'-(trifluoromethyl)spiro[1,3-dioxolane-2,7'-5,6-dihydrocyclopenta[c]pyridine] (650.0 mg, 1.51 mmol) in a mixture of 1,2-dimethoxyethane (15 mL) and water (5 mL) was treated with silver carbonate (416.7 mg, 1.51 mmol) and stirred at 85 ^oC overnight. The mixture was diluted with EtOAc and filtered through celite. The filtrate was concentrated to remove the dimethoxyethane. The residue was re-suspended in 60 mL of 1:1 EtOAc/H_2O and extracted with 3 x 15 mL EtOAc. The combined organics were rinsed with 10 mL of brine, dried with $MgSO_4$, filtered, and concentrated to dryness. Purification was achieved by chromatography on silica using 10-30% EtOAc/hexanes to afford 4'-(3,3-difluorocyclobutoxy)-1'-(trifluoromethyl)spiro[1,3-dioxolane-2,7'-5,6-dihydrocyclopenta[c]pyridine]-5'-ol as a solid (280 mg, 50%). ^1H NMR (400 MHz, $CDCl_3$): δ 8.11 (s, 1H), 5.39-5.32 (m, 1H), 4.97-4.87 (m, 1H), 4.33-4.20 (m, 2H), 4.17-4.04 (m, 2H), 3.27-3.13 (m, 2H), 2.96-2.75 (m, 2H), 2.63 (dd, 1H), 2.53 (d, 1H), 2.28 (dd, 1H).

Step D: Preparation of 4-(3,3-difluorocyclobutoxy)-1-(trifluoromethyl)spiro[cyclopenta[c]pyridine-7,2'-[1,3]dioxolan]-5(6H)-one. A solution of 4'-(3,3-difluorocyclobutoxy)-1'-(trifluoromethyl)spiro[1,3-dioxolane-2,7'-5,6-dihydrocyclopenta[c]pyridine]-5'-ol (280.0 mg, 0.76 mmol) in dichloromethane (10 mL) at 25 ^oC was treated with Dess-Martin

periodinane (500.0 mg, 1.18 mmol). After 2 h, the reaction was quenched by the addition of 10 mL of saturated $Na_2S_2O_3$ solution and 10 mL of saturated $NaHCO_3$ solution. The resulting biphase stirred for 10 min. The reaction mixture was poured into 20 mL of water and extracted with 3 x 20 mL CH_2Cl_2. The combined organics were rinsed with 10 mL of brine, dried with $MgSO_4$, filtered, and concentrated to dryness to afford 4'-(3,3-difluorocyclobutoxy)-1'-(trifluoromethyl)spiro[1,3-dioxolane-2,7'-6H-cyclopenta[c]pyridine]-5'-one as a solid (270 mg, 97%) that was used without further purification. LCMS ESI (+) (M+H) m/z 366.

Step E: Preparation of 4-(3,3-difluorocyclobutoxy)-6-fluoro-1-(trifluoromethyl)spiro[cyclopenta[c]pyridine-7,2'-[1,3]dioxolan]-5(6H)-one: A solution of 4'-(3,3-difluorocyclobutoxy)-1'-(trifluoromethyl)spiro[1,3-dioxolane-2,7'-6H-cyclopenta[c]pyridine]-5'-one (270 mg, 0.740 mmol) and triethylamine (410 uL, 2.96 mmol) in dichloromethane (10 mL) at 0 ^oC was treated with tert-butyl-dimethyl-(trifluoromethylsulfonyl)silane (480 uL, 2.22 mmol) and stirred at 0 ^oC for 30 min. The reaction mixture was left to stir over night at room temperature. The reaction mixture was poured into 10 mL of saturated $NaHCO_3$, stirred for 10 min, and extracted with 3 x 15 mL CH_2Cl_2. The combined organics were rinsed with 10 mL of brine, dried with $MgSO_4$, filtered, and concentrated to dryness. The unpurified residue was dissolved in acetonitrile (10 mL) and treated with 1-chloromethyl-4-fluoro-1,4-diazoniabicyclo[2.2.2]octane bis-(tetrafluoroborate) (322 mg, 0.92 mmol). The reaction stirred for 6 h at room temperature. Volatiles were removed by concentration under reduced pressure. The reaction mixture was poured into 30 mL of water and extracted with 3 x 15 mL EtOAc. The combined organics were rinsed with 10 mL of brine, dried with $MgSO_4$, filtered, and concentrated to dryness. Purification was achieved by chromatography on silica using 5-20% EtOAc/hexanes to afford 4'-(3,3-difluorocyclobutoxy)-6'-fluoro-1'-(trifluoromethyl)spiro[1,3-dioxolane-2,7'-6H-cyclopenta[c]pyridine]-5'-one as a white solid (180 mg, 56%). ^1H NMR (400 MHz, $CDCl_3$): δ 8.35 (s, 1H), 5.13 (d, 1H), 5.01-4.91 (m, 1H), 4.47-4.38 (m, 1H), 4.38-4.26 (m, 3H), 3.30-3.14 (m, 2H), 3.04-2.86 (m, 2H).

Step F: Preparation of (5R,6R)-4-(3,3-difluorocyclobutoxy)-6-fluoro-1-(trifluoromethyl)-5,6-dihydrospiro[cyclopenta[c]pyridine-7,2'-[1,3]dioxolan]-5-ol. A solution of 4'-(3,3-difluorocyclobutoxy)-6'-fluoro-1'-(trifluoromethyl)spiro[1,3-dioxolane-2,7'-6H-cyclopenta[c]pyridine]-5'-one (180 mg, 0.47 mmol) in dichloromethane (10 mL) was cooled to 0 ^oC and sparged with nitrogen for 5 min. During this time formic acid (53.1 uL, 1.41 mmol) and triethylamine (98.2 uL, 0.70 mmol) were sequentially added. Once sparging was complete, RuCl(p-cymene)[(*S*,*S*)-Ts-DPEN] (15.0 mg, 0.023 mmol) was added under a continuous stream of nitrogen. The reaction vessel was sealed and put into the refrigerator to react overnight. Volatiles were removed by concentration under reduced pressure. Purification was achieved by chromatography

on silica using 10-30% EtOAc/hexanes to afford (5'*R*,6'*R*)-4'-(3,3-difluorocyclobutoxy)-6'-fluoro-1'-(trifluoromethyl)spiro[1,3-dioxolane-2,7'-5,6-dihydrocyclopenta[c]pyridine]-5'-ol as a clear solid (152 mg, 84%). LCMS ESI (+) (M+H) m/z 386.

Step G: Preparation of (5S,6R)-4-(3,3-difluorocyclobutoxy)-6-fluoro-1-(trifluoromethyl)-5,6-dihydrospiro[cyclopenta[c]pyridine-7,2'-[1,3]dioxolan]-5-yl 4-nitrobenzoate. A solution of (5'*R*,6'*R*)-4'-(3,3-difluorocyclobutoxy)-6'-fluoro-1'-(trifluoromethyl)spiro[1,3-dioxolane-2,7'-5,6-dihydrocyclopenta[c]pyridine]-5'-ol (124.4 mg, 0.32 mmol), polymer supported triphenylphosphine (~2.06 mmol/g, 627.4 mg, 1.29 mmol), and 4-nitrobenzoic acid (215.9 mg, 1.29 mmol) in tetrahydrofuran (3.3 mL) was treated with diisopropyl azodicarboxylate (248 uL, 1.26 mmol) and stirred at 25 °C for 2 h. LCMS indicates product formation. The reaction mixture was filtered and the filter cake rinsed with 30 mL EtOAc. The filtrate was concentrated and purified by chromatography on silica using 10-25% EtOAc/hexanes to afford (5*S*,6*R*)-4-(3,3-difluorocyclobutoxy)-6-fluoro-1-(trifluoromethyl)-5,6-dihydrospiro[cyclopenta[*c*]pyridine-7,2'-[1,3]dioxolan]-5-yl 4-nitrobenzoate as a white solid (160.0 mg, 93%). LCMS ESI (+) (M+H) m/z 535.

Step H: Preparation of (5S,6R)-4-(3,3-difluorocyclobutoxy)-6-fluoro-1-(trifluoromethyl)-5,6-dihydrospiro[cyclopenta[c]pyridine-7,2'-[1,3]dioxolan]-5-ol. A solution of [(5'*S*,6'*R*)-4'-(3,3-difluorocyclobutoxy)-6'-fluoro-1'-(trifluoromethyl)spiro[1,3-dioxolane-2,7'-5,6-dihydrocyclopenta[c]pyridine]-5'-yl] 4-nitrobenzoate (194.0 mg, 0.36 mmol) in tetrahydrofuran (7 mL) at 25 °C was treated with a solution of freshly prepared hydroxylithium hydrate (16.8 mg, 0.40 mmol) in water (2.1 mL) and stirred at 25 °C for 30 min. An additional portion of hydroxylithium hydrate (8.4 mg, 0.20 mmol) in water (1.0 mL) was added and the reaction mixture stirred for another 30 minutes. 0.5 mL of saturated NH_4Cl was added and volatiles were removed under reduced pressure. The reaction mixture was poured into 10 mL of saturated $NaHCO_3$ and extracted with 3 x 15 mL EtOAc. The combined organics were rinsed with 10 mL of brine, dried with $MgSO_4$, filtered, and concentrated to dryness. Purification was achieved by chromatography on silica using 10-35% EtOAc/hexanes to afford (5*S*,6*R*)-4-(3,3-difluorocyclobutoxy)-6-fluoro-1-(trifluoromethyl)-5,6-dihydrospiro[cyclopenta[*c*]pyridine-7,2'-[1,3]dioxolan]-5-ol as a white solid (74.1 mg, 53%). LCMS ESI (+) (M+H) m/z 386.

Step I: Preparation of (5R,6S)-4-(3,3-difluorocyclobutoxy)-5,6-difluoro-1-(trifluoromethyl)-5,6-dihydrospiro[cyclopenta[c]pyridine-7,2'-[1,3]dioxolane]. A solution of (5'*S*,6'*R*)-4'-(3,3-difluorocyclobutoxy)-6'-fluoro-1'-(trifluoromethyl)spiro[1,3-dioxolane-2,7'-5,6-dihydrocyclopenta[c]pyridine]-5'-ol (74.1 mg, 0.19 mmol) in dichloromethane (3.8 mL) at 25 °C was treated with diethylaminosulfur trifluoride (50.8 uL, 0.38 mmol). The reaction mixture was allowed to stir for 30 minutes. The reaction mixture was quenched by the careful addition of 1 mL of aqueous

saturated $NaHCO_3$. The resulting mixture stirred for 30 min. The reaction mixture was poured into 20 mL of water and extracted with 3 x 15 mL CH_2Cl_2. The combined organics were rinsed with 10 mL of brine, dried with $MgSO_4$, filtered, and concentrated to dryness. Purification was achieved by chromatography on silica using 5-25% EtOAc/hexanes to afford (5*R*,6*S*)-4-(3,3-difluorocyclobutoxy)-5,6-difluoro-1-(trifluoromethyl)-5,6-dihydrospiro[cyclopenta[*c*]pyridine-7,2'-[1,3]dioxolane] as a white solid (72.0 mg, 97%). LCMS ESI (+) (M+H) m/z 388.

*Step J: Preparation of (5R,6S,7S)-4-(3,3-difluorocyclobutoxy)-5,6-difluoro-1-(trifluoromethyl)-6,7-dihydro-5H-cyclopenta[c]pyridin-7-ol (**27**).* A solution of (5'*R*,6'*S*)-4'-(3,3-difluorocyclobutoxy)-5',6'-difluoro-1'-(trifluoromethyl)spiro[1,3-dioxolane-2,7'-5,6-dihydrocyclopenta[c]pyridine] (72.0 mg, 0.19 mmol) in dichloromethane (4.0 mL) at 0 °C was treated with 70% aqueous perchloric acid (800 uL). The reaction mixture was heated to 44 °C for 5 h. The reaction mixture was cooled to 0 °C, carefully quenched with a mixture of 10 mL of saturated $NaHCO_3$ / 10 mL of water and extracted with 3 x 15 mL CH_2Cl_2. The combined organics were rinsed with 10 mL of brine, dried with $MgSO_4$, filtered, and concentrated to dryness. The product was used immediately without further purification by dissolving in 2 mL of MeOH, cooling to 0 °C, and treating with sodium borohydride (7.0 mg, 0.19 mmol). The reaction stirred for 15 min and was then quenched by the addition of 1 mL of saturated NH_4Cl. Volatiles were removed by concentration under reduced pressure. The reaction mixture was poured into 20 mL of water and extracted with 3 x 15 mL EtOAc. The combined organics were rinsed with 10 mL of brine, dried with $MgSO_4$, filtered, and concentrated to dryness. Purification was achieved by chromatography on silica using 10-40% EtOAc/hexanes to afford (5*R*,6*S*,7*S*)-4-(3,3-difluorocyclobutoxy)-5,6-difluoro-1-(trifluoromethyl)-6,7-dihydro-5*H*-cyclopenta[*c*]pyridin-7-ol (**27**) as a white solid (53.0 mg, 83%). Data for (5*R*,6*S*,7*S*)-4-(3,3-difluorocyclobutoxy)-5,6-difluoro-1-(trifluoromethyl)-6,7-dihydro-5*H*-cyclopenta[*c*]pyridin-7-ol (**27**): Retention time HPLC (14 min) = 3.37 min; LCMS ESI (+) (M+H) m/z 346; ^{1}H NMR (400 MHz, $CDCl_3$): δ 8.24 (s, 1H), 5.94 (ddd, J = 54.0, 4.5, 1.5 Hz, 1H), 5.48 – 5.39 (m, 1H), 5.07 (ddt, J = 47.8, 16.0, 4.8 Hz, 1H), 4.96 – 4.87 (m, 1H), 3.31 – 3.13 (m, 2H), 3.01 – 2.78 (m, 2H), 2.56 – 2.47 (m, 1H). ^{13}C NMR (101 MHz, $CDCl_3$) δ 152.51, 139.18 (q, J = 37.1 Hz), 136.99 (t, J = 3.9 Hz), 134.54, 134.20 (dd, J = 16.3, 4.1 Hz), 122.28 (q, J = 273.9 Hz), 117.06 (dd, J = 283.1, 270.2 Hz), 88.33 (ddd, J = 292.0, 16.9, 11.7 Hz), 86.35 (dt, J = 273.3, 16.9 Hz), 70.41 (dd, J = 18.9, 7.9 Hz), 63.97 – 63.25 (m), 43.77 – 42.85 (m).^{19}F NMR (376 MHz, $CDCl_3$) δ -64.61 (s, 3F), -84.36 – -85.21 (m, 1F), -95.59 – -96.37 (m, 1F), -187.20 (ddd, J = 54.1, 16.0, 6.7 Hz, 1F), -212.58 – -212.95 (m, 1F).

Supplementary information

Data including statistics for X-ray data (Table S1), tabulated LCMS data for the library examples **1-5** and **7-13** (Table S2), HPLC traces for **24** and **27**, NMR spectra for **27** (^{1}H, ^{13}C, ^{19}F), summary of computational methods, visualization of electrostatic surface potentials (for **7**, **13** and **14**), and complete synthetic procedures for missing compounds is available in the supplementary information file.

Compliance with ethical standards

Conflict of Interest The authors declare the following competing financial interests: S.Y. is a shareholder and former employee of Merck. The remaining authors were employees of Peloton Therapeutics and possibly shareholders entitling them to potential milestone payments based on the clinical success of MK-6482/Belzutifan.

Author Contributions

The manuscript was written with the help and contributions from all authors. All authors have given approval of the manuscript.

Abbreviations used

AIBN, azobisisobutyronitrile; ARNT, aryl hydrocarbon receptor nuclear translocator; BID, twice daily; CCND1, cyclin D1; ccRCC, clear-cell renal cell carcinoma; DAST, diethylaminosulfur trifluoride; DIAD, diisopropyl azodicarboxylate; DPEN, 1,2-diphenyl-1,2-ethylenediamine; ESP, electrostatic potential; Fsp^3, fraction of sp^3 hybridized carbons; F-TEDA-BF_4, 1-chloromethyl-4-fluoro-1,4-diazoniabicyclo[2.2.2]octane bis-(tetrafluoroborate);HIFα, hypoxia inducible factor α; HREs, hypoxia-response elements; MDCK-MDR1, Madin−Darby canine kidney epithelial cells expressing Multi-Drug Resistance Gene 1; NBS, *N*-bromosuccinimide; PAS-B*, Per-Arnt-Sim-B*; PHDs, prolyl-hydroxylases; PK/PD, pharmacokinetic/pharmacodynamic; PMB, para-

methoxybenzyl; PPTS, pyridinium para-toluenesulfonate; pVHL, VHL protein; qPCR, quantitative polymerase chain reaction; RCC, renal cell carcinoma; RP2D, recommended phase 2 dose; Selectfluor®, 1-Chloromethyl-4-fluoro-1,4-diazoniabicyclo[2.2.2]octane bis(tetrafluoroborate); SPA, scintillation proximity assay; TBS, tert-butyldimethylsilyl; TMP, 2,2,6,6-tetramethyl-piperidine; UGT, UDP-glucuronyltransferase; VEGFA, vascular endothelial growth factor A; VHL, von Hippel-Lindau.

References

1. Choueiri TK, Longo DL, Motzer RJ. Systemic Therapy for Metastatic Renal-Cell Carcinoma. New England Journal of Medicine. 2017;376(4):354-66. doi:10.1056/NEJMra1601333.
2. Kidney and Renal Pelvis Cancer. In: Cancer Stat Facts. National Cancer Institute. 2022. https://seer.cancer.gov/statfacts/html/kidrp.html. Accessed March 3 2023.
3. Sato Y, Yoshizato T, Shiraishi Y, Maekawa S, Okuno Y, Kamura T et al. Integrated molecular analysis of clear-cell renal cell carcinoma. Nature Genetics. 2013;45(8):860-7. doi:10.1038/ng.2699.
4. Jaakkola P, Mole DR, Tian Y-M, Wilson MI, Gielbert J, Gaskell SJ et al. Targeting of HIF-α to the von Hippel-Lindau Ubiquitylation Complex by O2 - Regulated Prolyl Hydroxylation. Science. 2001;292(5516):468-72. doi:10.1126/science.1059796.
5. Bruick RK, McKnight SL. A Conserved Family of Prolyl-4-Hydroxylases That Modify HIF. Science. 2001;294(5545):1337-40. doi:10.1126/science.1066373.
6. Wang GL, Jiang BH, Rue EA, Semenza GL. Hypoxia-inducible factor 1 is a basic-helix-loop-helix-PAS heterodimer regulated by cellular O2 tension. Proceedings of the National Academy of Sciences. 1995;92(12):5510-4. doi:10.1073/pnas.92.12.5510.
7. Tian H, McKnight SL, Russell DW. Endothelial PAS domain protein 1 (EPAS1), a transcription factor selectively expressed in endothelial cells. Genes & Development. 1997;11(1):72-82. doi:10.1101/gad.11.1.72.
8. Gu YZ, Moran SM, Hogenesch JB, Wartman L, Bradfield CA. Molecular characterization and chromosomal localization of a third alpha-class hypoxia inducible factor subunit, HIF3alpha. Gene Expr. 1998;7(3):205-13.
9. Diao X, Ye F, Zhang M, Ren X, Tian X, Lu J et al. Identification of oleoylethanolamide as an endogenous ligand for HIF-3α. Nature Communications. 2022;13(1). doi:10.1038/s41467-022-30338-z.
10. Kaelin WG, Ratcliffe PJ. Oxygen Sensing by Metazoans: The Central Role of the HIF Hydroxylase Pathway. Molecular Cell. 2008;30(4):393-402. doi:10.1016/j.molcel.2008.04.009.
11. Majmundar AJ, Wong WJ, Simon MC. Hypoxia-Inducible Factors and the Response to Hypoxic Stress. Molecular Cell. 2010;40(2):294-309. doi:10.1016/j.molcel.2010.09.022.
12. Keith B, Johnson RS, Simon MC. HIF1α and HIF2α: sibling rivalry in hypoxic tumour growth and progression. Nature Reviews Cancer. 2011;12(1):9-22. doi:10.1038/nrc3183.
13. Zimmer M, Doucette D, Siddiqui N, Iliopoulos O. Inhibition of Hypoxia-Inducible Factor Is Sufficient for Growth Suppression of VHL−/− Tumors. Molecular Cancer Research. 2004;2(2):89-95. doi:10.1158/1541-7786.89.2.2.

14. Kondo K, Klco J, Nakamura E, Lechpammer M, Kaelin WG. Inhibition of HIF is necessary for tumor suppression by the von Hippel-Lindau protein. Cancer Cell. 2002;1(3):237-46. doi:10.1016/s1535-6108(02)00043-0.
15. Kondo K, Kim WY, Lechpammer M, Kaelin WG. Inhibition of HIF2α Is Sufficient to Suppress pVHL-Defective Tumor Growth. PLoS Biology. 2003;1(3). doi:10.1371/journal.pbio.0000083.
16. Maranchie JK, Vasselli JR, Riss J, Bonifacino JS, Linehan WM, Klausner RD. The contribution of VHL substrate binding and HIF1-α to the phenotype of VHL loss in renal cell carcinoma. Cancer Cell. 2002;1(3):247-55. doi:10.1016/s1535-6108(02)00044-2.
17. Monzon FA, Alvarez K, Peterson L, Truong L, Amato RJ, Hernandez-McClain J et al. Chromosome 14q loss defines a molecular subtype of clear-cell renal cell carcinoma associated with poor prognosis. Modern Pathology. 2011;24(11):1470-9. doi:10.1038/modpathol.2011.107.
18. Shen C, Beroukhim R, Schumacher SE, Zhou J, Chang M, Signoretti S et al. Genetic and Functional Studies Implicate HIF1α as a 14q Kidney Cancer Suppressor Gene. Cancer Discovery. 2011;1(3):222-35. doi:10.1158/2159-8290.Cd-11-0098.
19. Scheuermann TH, Tomchick DR, Machius M, Guo Y, Bruick RK, Gardner KH. Artificial ligand binding within the HIF2α PAS-B domain of the HIF2 transcription factor. Proceedings of the National Academy of Sciences. 2009;106(2):450-5. doi:10.1073/pnas.0808092106.
20. Scheuermann TH, Li Q, Ma H-W, Key J, Zhang L, Chen R et al. Allosteric inhibition of hypoxia inducible factor-2 with small molecules. Nature Chemical Biology. 2013;9(4):271-6. doi:10.1038/nchembio.1185.
21. Rogers JL, Bayeh L, Scheuermann TH, Longgood J, Key J, Naidoo J et al. Development of Inhibitors of the PAS-B Domain of the HIF-2α Transcription Factor. Journal of Medicinal Chemistry. 2013;56(4):1739-47. doi:10.1021/jm301847z.
22. Scheuermann TH, Stroud D, Sleet CE, Bayeh L, Shokri C, Wang H et al. Isoform-Selective and Stereoselective Inhibition of Hypoxia Inducible Factor-2. Journal of Medicinal Chemistry. 2015;58(15):5930-41. doi:10.1021/acs.jmedchem.5b00529.
23. Wu D, Su X, Lu J, Li S, Hood BL, Vasile S et al. Bidirectional modulation of HIF-2 activity through chemical ligands. Nature Chemical Biology. 2019;15(4):367-76. doi:10.1038/s41589-019-0234-5.
24. Wallace EM, Rizzi JP, Han G, Wehn PM, Cao Z, Du X et al. A Small-Molecule Antagonist of HIF2α Is Efficacious in Preclinical Models of Renal Cell Carcinoma. Cancer Research. 2016;76(18):5491-500. doi:10.1158/0008-5472.Can-16-0473.
25. Cho H, Du X, Rizzi JP, Liberzon E, Chakraborty AA, Gao W et al. On-target efficacy of a HIF-2α antagonist in preclinical kidney cancer models. Nature. 2016;539(7627):107-11. doi:10.1038/nature19795.
26. Wehn PM, Rizzi JP, Dixon DD, Grina JA, Schlachter ST, Wang B et al. Design and Activity of Specific Hypoxia-Inducible Factor-2α (HIF-2α) Inhibitors for the Treatment of Clear Cell Renal Cell Carcinoma: Discovery of Clinical Candidate (S)-3-((2,2-Difluoro-1-hydroxy-7-(methylsulfonyl)-2,3-dihydro-1H-inden-4-yl)oxy)-5-fluorobenzonitrile (PT2385). Journal of Medicinal Chemistry. 2018;61(21):9691-721. doi:10.1021/acs.jmedchem.8b01196.
27. Courtney KD, Infante JR, Lam ET, Figlin RA, Rini BI, Brugarolas J et al. Phase I Dose-Escalation Trial of PT2385, a First-in-Class Hypoxia-Inducible Factor-2α Antagonist in Patients With Previously Treated Advanced Clear Cell Renal Cell Carcinoma. Journal of Clinical Oncology. 2018;36(9):867-74. doi:10.1200/jco.2017.74.2627.
28. Xu R, Wang K, Rizzi JP, Huang H, Grina JA, Schlachter ST et al. 3-[(1S,2S,3R)-2,3-Difluoro-1-hydroxy-7-methylsulfonylindan-4-yl]oxy-5-fluorobenzonitrile (PT2977), a Hypoxia-Inducible Factor 2α (HIF-2α) Inhibitor for the Treatment of Clear Cell Renal Cell Carcinoma. Journal of Medicinal Chemistry. 2019;62(15):6876-93. doi:10.1021/acs.jmedchem.9b00719.

29. Trial search results for MK-6482. In: Clinical Trials.gov. U.S. National Library of Medicine. 2023. https://clinicaltrials.gov/ct2/results?cond=&term=MK-6482&cntry=&state=&city=&dist. Accessed March 8 2023.
30. Search results for MK-6482. American Society of Clinical Oncology, Journal of Clinical Oncology. 2023. https://ascopubs.org/action/doSearch?SeriesKey=jco&AllField=MK-6482&ConceptID=&startPage=&sortBy=Ppub. Accessed March 8 2023.
31. FDA approves belzutifan for cancers associated with von Hippel-Lindau disease. U.S. Food & Drug Administration, FDA.gov. 2021. https://www.fda.gov/drugs/resources-information-approved-drugs/fda-approves-belzutifan-cancers-associated-von-hippel-lindau-disease. Accessed March 8 2023.
32. Jonasch E, Donskov F, Iliopoulos O, Rathmell WK, Narayan VK, Maughan BL et al. Belzutifan for Renal Cell Carcinoma in von Hippel–Lindau Disease. New England Journal of Medicine. 2021;385(22):2036-46. doi:10.1056/NEJMoa2103425.
33. Lovering F, Bikker J, Humblet C. Escape from Flatland: Increasing Saturation as an Approach to Improving Clinical Success. Journal of Medicinal Chemistry. 2009;52(21):6752-6. doi:10.1021/jm901241e.
34. Pennington LD, Moustakas DT. The Necessary Nitrogen Atom: A Versatile High-Impact Design Element for Multiparameter Optimization. Journal of Medicinal Chemistry. 2017;60(9):3552-79. doi:10.1021/acs.jmedchem.6b01807.
35. Singh SK, Das A. The n → π* interaction: a rapidly emerging non-covalent interaction. Physical Chemistry Chemical Physics. 2015;17(15):9596-612. doi:10.1039/c4cp05536e.
36. Dixon DD, Grina J, Josey JA, Rizzi JP, Schlachter ST, Wallace EM et al., inventors; Aromatic compounds and uses thereof WIPO patent WO2016144825A1. September 15, 2016.
37. Hansch C, Leo A, Taft RW. A survey of Hammett substituent constants and resonance and field parameters. Chemical Reviews. 1991;91(2):165-95. doi:10.1021/cr00002a004.
38. Ouzzine M, Barré L, Netter P, Magdalou J, Fournel-Gigleux S. The Human UDP-Glucuronosyltransferases: Structural Aspects and Drug Glucuronidation. Drug Metabolism Reviews. 2003;35(4):287-303. doi:10.1081/dmr-120026397.
39. Jain A, Ramanathan V, Sankararamakrishnan R. Lone pair ···π interactions between water oxygens and aromatic residues: Quantum chemical studies based on high-resolution protein structures and model compounds. Protein Science. 2009:NA-NA. doi:10.1002/pro.67.
40. Stavber S, Jereb M, Zupan M. SelectfluorTM F-TEDA-BF4 mediated and solvent directed iodination of aryl alkyl ketones using elemental iodineElectronic supplementary information (ESI) available: experimental details. See http://www.rsc.org/suppdata/cc/b2/b200240j. Chemical Communications. 2002(5):488-9. doi:10.1039/b200240j.
41. Cheung CW, Buchwald SL. Palladium-Catalyzed Hydroxylation of Aryl and Heteroaryl Halides Enabled by the Use of a Palladacycle Precatalyst. The Journal of Organic Chemistry. 2014;79(11):5351-8. doi:10.1021/jo500662s.
42. Ros A, Magriz A, Dietrich H, Fernández R, Alvarez E, Lassaletta JM. Enantioselective Synthesis of Vicinal Halohydrins via Dynamic Kinetic Resolution. Organic Letters. 2005;8(1):127-30. doi:10.1021/ol052821k.
43. Ji Y, Brueckl T, Baxter RD, Fujiwara Y, Seiple IB, Su S et al. Innate C-H trifluoromethylation of heterocycles. Proceedings of the National Academy of Sciences. 2011;108(35):14411-5. doi:10.1073/pnas.1109059108.

Supplementary Files

This is a list of supplementary files associated with this preprint. Click to download.

- ExpandedExperimentalCF3PyridineMCR.pdf